

Multi-Layered Dual-Band Dual-Polarized Reflectarray Design  
Toward Rim-Located Reconfigurable Reflectarrays for  
Interference Mitigation in Reflector Antennas

Trisha Bora

Thesis submitted to the Faculty of the  
Virginia Polytechnic Institute and State University  
in partial fulfillment of the requirements for the degree of

Master of Science  
in  
Electrical Engineering

Jordan Budhu, Chair  
Steven W. Ellingson  
Majid Manteghi

May 7, 2024  
Blacksburg, Virginia

Keywords: Electromagnetics, Dual-band/Wide-band Reflectarray, Antennas, Interference  
Mitigation

Copyright 2024, Trisha Bora

# Multi-Layered Dual-Band Dual-Polarized Reflectarray Design Toward Rim-Located Reconfigurable Reflectarrays for Interference Mitigation in Reflector Antennas

Trisha Bora

(ABSTRACT)

The rise of satellites in Low Earth Orbit (LEO) is causing more terrestrial electromagnetic interference in the important L- and X-band frequencies which are crucial for astronomical observations. This thesis introduces a reflectarray design which can serve as a basis for an interference mitigation solution for radio telescopes. In the envisioned application, when the reflectarray is placed around the circumference of an existing radio telescope, it can drive a null into the radio telescopes radiation pattern sidelobe distribution. Since the reflectarray only occupies a small portion of the rim of the paraboloidal main reflector, its presence does not significantly affect the main lobe peak gain. Since Iridium and Starlink are the target mega-constellations, the reflectarray must be dual band. To cover the operational bandwidths of these constellations, the target bandwidth in the L-band (Iridium) is 0.7%, and that in the X-band (Starlink) is 17.1%. This makes the design of the reflectarray challenging as the frequencies are widely separated and the bandwidth in the X-band is wide. The work of this thesis marks a first step in this effort. It includes a reflectarray design containing a multi-layer stack consisting of: (1) a grounded substrate, (2) an X-band slot loaded unit cell geometry, (3) a dielectric superstrate, and (4) an L-band layer containing crossed dipoles. The dual band reflectarray is dual linearly polarized to maintain symmetric response. The reflectarray is designed and simulated using full-wave solvers. The results show that the reflectarray designs are capable of pattern shaping at both bands and operate across the required bandwidths. This architecture could serve as a basis for future

reflectarrays capable of nulling satellite interference from mega-constellations in observatory applications in the future.

# Multi-Layered Dual-Band Dual-Polarized Reflectarray Design Toward Rim-Located Reconfigurable Reflectarrays for Interference Mitigation in Reflector Antennas

Trisha Bora

(GENERAL AUDIENCE ABSTRACT)

The signal clarity issues stemming from the increasing number of satellites in Low Earth Orbit (LEO), particularly in the vital L- and X-band frequencies essential for global communications and radio astronomy, are the motivation of this thesis. The endeavor concentrates on designing a dual-band dual-polarized reflectarray antenna which may ultimately be used to help mitigate interference in these bands in radio telescopes. The work is focused on the frequency ranges utilized by the major satellite networks Iridium and Starlink, which operate within the L-band (1616-1626.5 MHz) and X-band (10.7-12.7 GHz). Recognizing the significance of these frequencies for global communication and also to radio astronomy, the reflectarray is designed to contribute to an interference mitigation system which would ultimately allow for coexistence between radio telescopes and communications systems satellites. Targeting bandwidth achievements of 0.7% for the L-band and 17.1% for the X-band, the focus is on nulling interference arising across these frequency bands and thereby increasing the sensitivity of the radio telescope operating amongst these mega-constellations. The thesis documents a multilayered reflectarray antenna, containing a wide-band X-band layer of slot antennas on one layer and an L-band superstrate layer containing crossed dipoles at another, both of which utilize dual linear polarization for symmetric operation. The completed reflectarray can operate simultaneously in both bands. It has been shown in [5, 7] that reflectarrays placed along the rim of radio telescopes main reflector can be used to drive nulls in the sidelobe envelope of its radiation pattern thereby nulling incoming interference. The

antenna design of this thesis suggests a possible candidate for these interference mitigation systems where both bands are targeted.

# Dedication

*This thesis is dedicated to my family who have always supported me and helped me at every point in my life.*

# Acknowledgments

This work was supported in part by National Science Foundation grant AST-2128506.

My appreciation goes to Dr. Jordan Budhu, my thesis chair, for his guidance, patience, and expertise. I am grateful to my committee members, Dr. Majid Mantegi and Dr. Steven Ellingson, for sparing their valuable time and serving on my M.S. Thesis Advisory Committee. I extend my thanks to all the professors who have contributed to my graduate experience through their coursework. I would like to express my gratitude to the administration and all related staff for their dedication and hard work behind the scenes at Virginia Tech.

I extend my gratitude to my parents for their unwavering support throughout this journey. A special shoutout to my mom, who has been my rock during times when I was at my lowest. I also want to express my deep appreciation to my dad, who has supported me in his own unique way. Equally, I am thankful for the encouragement and support from my little brother, whose presence have been a constant source of motivation and joy. I am thankful to my relatives and friends in India for their constant encouragement. Special recognition is given to Dr. Saradindu Ghosh, my undergraduate advisor, whose support has been instrumental in my academic development, continuing through my graduate experience. I also acknowledge Dr. Partha Pratim Talukdar for his advisement and patience with me.

To my friends at Virginia Tech, I am grateful for the experiences and discussions we've shared, which have enriched my time at the university. My lab mates deserve a word of thanks for their collaboration, making the research process both productive and engaging. Your partnership has been appreciated. Finally, my roommates who have provided a supportive living environment, offering both encouragement and understanding. I am thankful to everyone who has been a part of this journey.

# Contents

<b>List of Figures</b>	<b>xi</b>
<b>List of Tables</b>	<b>xiv</b>
<b>1 Introduction</b>	<b>1</b>
1.1 Organization of the Thesis . . . . .	3
<b>2 Introduction to Reflectarray Operating Principles</b>	<b>5</b>
2.1 Introduction . . . . .	5
2.2 Geometry of the Parabolic Reflector . . . . .	6
2.2.1 Raised Cosine Feed Model . . . . .	8
2.2.2 Far-Zone Electric Field of a Parabolic Reflector . . . . .	10
2.3 Reflectarray Antenna Functionality . . . . .	15
2.4 Design Principles of Wide-band Reflectarray Elements . . . . .	16
2.5 Dual-Band and Dual-Polarized Performance Objectives . . . . .	19
<b>3 Unit Cell Design and Reflectarray Design at X-Band</b>	<b>21</b>
3.1 Unit Cell Design at X-Band . . . . .	21
3.1.1 Unit Cell Geometry . . . . .	22
3.1.2 Unit Cell Simulation Setup . . . . .	23
3.1.3 Unit Cell Simulation Results and Discussions . . . . .	24

3.2	Reflectarray Design at X-Band . . . . .	27
3.2.1	Design of the Reflectarray . . . . .	28
3.2.2	Reflectarray Simulation . . . . .	30
3.3	Impact of Superstrate on X-Band Layer Performance . . . . .	32
3.3.1	Unit Cell and Reflectarray Design with Superstrate . . . . .	32
3.3.2	Far-field Performance of the Reflectarray with Superstrate . . . . .	35
<b>4</b>	<b>Unit Cell and Reflectarray Design at L-Band</b>	<b>37</b>
4.1	L-Band Unit Cell . . . . .	37
4.1.1	Design Considerations for L-Band Operation . . . . .	37
4.1.2	Phase Range Analysis of the Cross Dipole at 1.62 GHz . . . . .	39
4.2	Design of the Cross Dipole Antenna Reflectarray . . . . .	40
4.2.1	Cross Dipole Reflectarray Working and Simulation . . . . .	41
<b>5</b>	<b>Results and Discussions</b>	<b>44</b>
5.1	Integration of the X-Band Layer to the L-Band Reflectarray at 1.62 GHz . . . . .	44
5.1.1	Simulation with the Slots without Homogenization . . . . .	44
5.1.2	Phase Analysis with Variable Slot Sizes . . . . .	45
5.1.3	Homogenization of the Lower X-Band Layer as an Impedance Sheet . . . . .	46
5.1.4	Design and Simulation of the Reflectarray with the Cross Dipoles and Homogenized Sheet . . . . .	50
5.2	Integration of the L-Band Layer to the X-Band Reflectarray at 11 GHz . . . . .	52

5.2.1	Design and Simulation of the Reflectarray with the Cross Dipole and Slot-Loaded Patches . . . . .	53
5.2.2	Far-Field Performance . . . . .	54
5.2.3	System Performance . . . . .	55
<b>6</b>	<b>Conclusion and Future Scope</b>	<b>57</b>
6.1	Summary of this Thesis Contribution . . . . .	57
6.2	Future Scope . . . . .	58
	<b>Appendices</b>	<b>59</b>
	<b>Appendix A Phases Requirements for the Reflectarray Designs</b>	<b>60</b>
A.1	Phase for the Reflectarray Design without Superstrate at X-Band . . . . .	60
A.2	Phase for the Reflectarray Design at L-Band . . . . .	62
	<b>Bibliography</b>	<b>64</b>

# List of Figures

1.1	3D model showing rim scattering reflectarray from [5]	2
2.1	Geometrical representation of the parabolic reflector and the subtended angle $\theta_0$ . from [2]	6
2.2	Parabolic reflector in 2D and 3D	7
2.3	Normal vector of the reflector	8
2.4	Example of Q feed ( $q=1.4$ )	10
2.5	The far-field reflector geometry from [2]	11
2.6	The co-polarized and cross-polarized directivity patterns	14
2.7	The design principle of a reflectarray	15
2.8	An E-shaped patch antenna design with marked dimensions from [25].	17
2.9	Phase response of the E-shaped patch antenna corresponding to variations in arm length.	18
2.10	An antenna design example configured for dual-band and dual-polarized operation.	19
2.11	Raised cosine q feed model scattering at 11 GHz	20
3.1	Unit cell geometry	22
3.2	Unit cell with periodic boundaries	23
3.3	Unit cell simulation setup	24

3.4	S-curve at 11 GHz . . . . .	25
3.5	S-curves at various incident angles . . . . .	26
3.6	S-curves at various frequencies . . . . .	27
3.7	Reflectarray design geometry . . . . .	28
3.8	S-curve at 11 GHz . . . . .	29
3.9	Analytical reflectarray construction at 11 GHz . . . . .	29
3.10	Reflectarray at X-band and simulation setup . . . . .	30
3.11	Co-polarized far fields at X-band for various frequencies . . . . .	31
3.12	The unit cell with superstrate . . . . .	33
3.13	S-curves of the unit cell with superstrate . . . . .	34
3.14	Analytical reflectarray construction with superstrate at 11 GHz . . . . .	34
3.15	Reflectarray with superstrate . . . . .	35
3.16	Co-polarized fields at X-band with superstrate . . . . .	36
4.1	L-band (Cross Dipole) unit cell . . . . .	38
4.2	S-curve at 1.62 GHz . . . . .	39
4.3	Analytical reflectarray model with the cross dipoles . . . . .	41
4.4	Simulation of the cross dipole reflectarray model . . . . .	42
4.5	Co-polarized radiation pattern of cross dipole array model . . . . .	43
5.1	Dipole with slot-loaded unit cells at L band . . . . .	45
5.2	Phase response variation at 1.62 GHz with changes in the slot size of the X-band geometry. . . . .	46

5.3	Slot-loaded unit cell conversion to Transmission line problem. . . . .	47
5.4	Impedance variation with the slot length . . . . .	49
5.5	Dipole antenna with X-band layer for one unit cell at L band . . . . .	49
5.6	Comparison of the S-curves containing the slot-loaded unit cells and homogenized sheet. . . . .	50
5.7	Reflectarray with cross dipole and homogenized sheet . . . . .	51
5.8	Comparison of the far-field patterns with and without the homogenized impedance sheet beneath the cross dipole reflectarray model. . . . .	52
5.9	Simulation model illustrating the cross dipole antenna over the $15 \times 15$ X-band unit cell patch array at 11 GHz. . . . .	53
5.10	Comparison of the far-field patterns with and without the cross dipole antenna on the superstrate of the slot-loaded reflectarray . . . . .	54

# List of Tables

2.1	E-shaped Patch Antenna Design Parameters . . . . .	18
3.1	Geometric Parameters of the Unit Cell . . . . .	23
3.2	Geometric Parameters of the Unit Cell with superstrate . . . . .	33
4.1	Geometric Parameters of the L-Band Unit Cell . . . . .	39
5.1	Reflectarray System Directivity and Efficiency . . . . .	56
A.1	Reflectarray Phase Distribution without the Superstrate at X-Band . . . . .	61
A.2	Reflectarray Phase Distribution at L-Band . . . . .	63

# Chapter 1

## Introduction

Satellites, crucial for global communications, especially through Iridium and Starlink networks, have been deployed to ensure connectivity in the most remote regions. With plans for expanding these satellite constellations, a worldwide continuous, broadband, low-latency internet service is anticipated. The number of satellites orbiting the Earth in low-earth orbit (LEO) is expected to see a tenfold increase in the coming years, aiming to provide coverage over every part of the planet.

However, this expansion poses significant interference challenges for radio astronomy, which relies on the clarity of signals from space. Two main issues have been identified: the interference from satellite frequencies close to those used in radio astronomy and the necessity for astronomers to conduct observations outside their designated frequency bands due to factors like the Doppler shift. These challenges, previously manageable, have grown with the increasing satellite numbers, complicating observations both within and outside designated bands.

In response to this dilemma, a new technology that could be used to enable mitigation of interference from satellite systems to radio astronomy was proposed: Electronically Reconfigurable Surfaces (ERS). This concept, introduced in [7] and expanded upon in [5], is illustrated in figure 1.1.

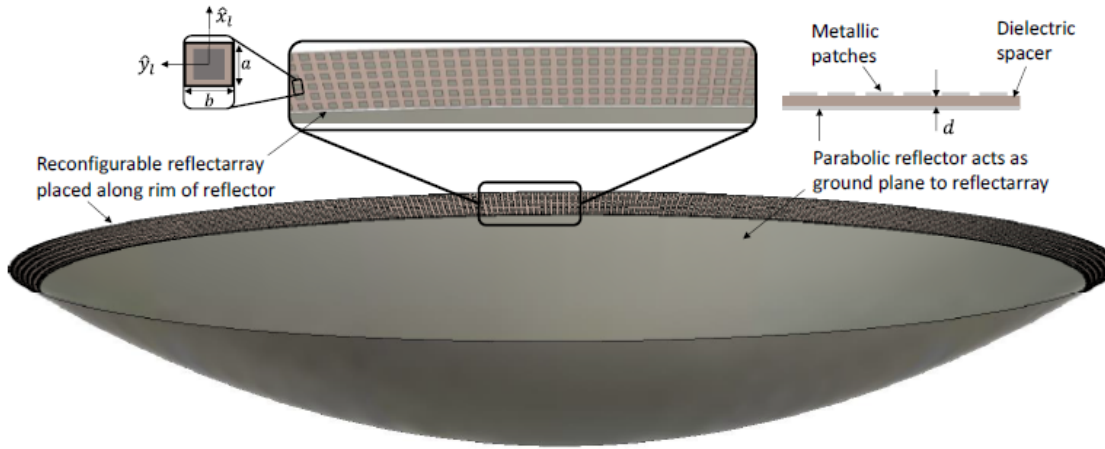


Figure 1.1: 3D model showing rim scattering reflectarray from [5]

An existing high gain reflector telescope is augmented with an ERS placed around its rim. A reflector antenna system equipped with an ERS is able to dynamically modify its spatial sidelobes by placing nulls in the direction of incoming interfering signals. The work in [7] modeled the ERS as physical optics (PO) plate scattering and provided proof of concept through simulation. The work in [6] then demonstrated practical ERS element state solving methods, including the desirable capability to constrain the main lobe gain and shape while simultaneously placing nulls in the direction of incoming interferers. In [14], the concept in [7] was shown to also work when the Electronically Reconfigurable Surface (ERS) was implemented using planar non-reconfigurable reflectarray placed along the outside of the reflector rim. Then [5] showed through full-wave simulation that the ERS can be realized as a conformal reconfigurable reflectarray. That work considered reconfigurable unit cells which operated at a single frequency in the L-band. The intent of the work of this thesis is to design a unit cell which can simultaneously work in both the L and X bands. As a first step, the design in this thesis is non-reconfigurable. It is the hope that future work can extend the designs to reconfigurable ones. Therefore, this thesis aims to design and evaluate a dual band static reflectarray which could potentially be used as a basis for a dual-band reconfigurable reflectarray for interference mitigation in radio telescopes in the

future. The dual-band reflectarray is designed to operate across popular satellite system frequency bands, notably Iridium and Starlink, by concentrating on two primary frequency ranges: 1616 to 1626.5 MHz, attributed to Iridium’s L-band operations, and 10.7 to 12.7 GHz, identified with Starlink’s X-band services. Thus, the design objectives include attaining the designated bandwidth goals—0.7% for the L-band and 17.1% for the X-band from the same reflecting aperture. These values are critical as they ensure the system’s capability to manage the full spectrum of signals potentially leading to interference from these satellite systems.

## 1.1 Organization of the Thesis

The organization of this thesis is as follows:

1. **Chapter 2: Fundamentals of Parabolic Reflectors and Reflectarray Antennas:** First we will lay a theoretical foundation by studying the predecessor of the reflectarray antenna, namely, the parabolic reflector antenna. We then link the focusing principles of parabolic reflector antennas to the design of reflectarray antennas. The necessity for dual-band, dual-polarized unit cells will be introduced.
2. **Chapter 3: X-Band Reflectarray Design:** Next, a wideband reflectarray operating across part of the X-band will be designed. The design also considers the effect of the integration of a superstrate layer which will ultimately support the L-band elements.
3. **Chapter 4: L-Band Reflectarray Design:** Chapter 4 will then focus on the design of a reflectarray which works in the L-band, using cross dipoles as reflecting elements.
4. **Chapter 5: Integration of L and X Band Layers Into A Single Aperture:** Chapter 5 will describe the integration of the X and L band layers into a single aperture. In this chapter the reflectarray’s performance is evaluated through full-wave simulation

at both bands.

5. **Chapter 6: Conclusion and Future Scope:** The thesis will conclude with a summary of the contributions of the work and provide suggestions for future research directions.

# Chapter 2

## Introduction to Reflectarray

### Operating Principles

#### 2.1 Introduction

A class of antenna that utilizes arrays of tunable elementary antennas embedded into a reflecting surface is called a *Reflectarray antenna*. A *reflectarray antenna* combines the advantages of parabolic reflector antennas (collimation or focusing) and phased arrays (tunable aperture field distributions) while avoiding the drawbacks (bulky paraboloids and lossy feed networks of phased arrays). These properties allow the reflectarray to focus fields or alter their direction without any mechanical movement, making it an efficient choice for applications requiring high directionality, such as satellite communications and radar systems, but with lower cost and complexity than phased arrays. Thus, the study of *parabolic reflectors* is useful for the understanding of reflectarray antennas. The following review of reflector antennas is referenced from the following references [3] and [26].

## 2.2 Geometry of the Parabolic Reflector

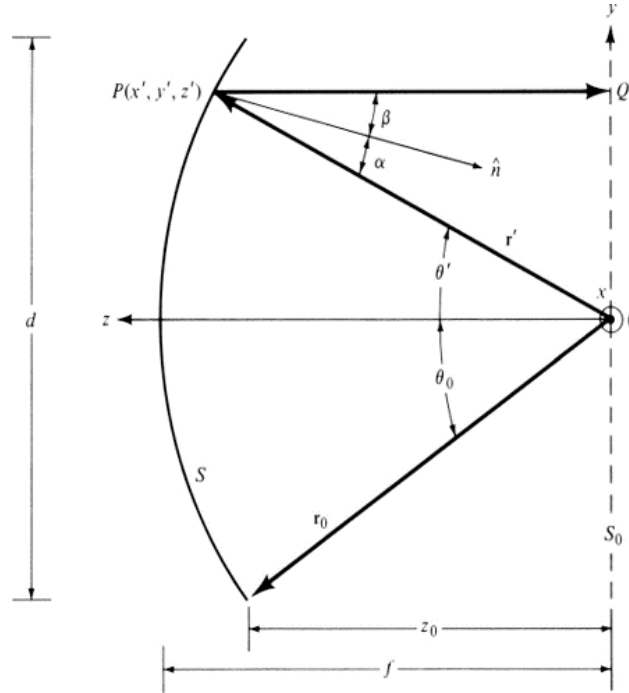
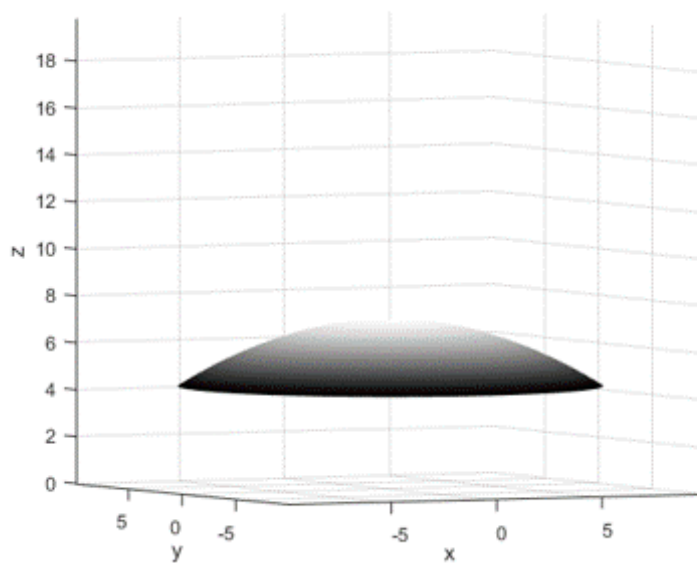
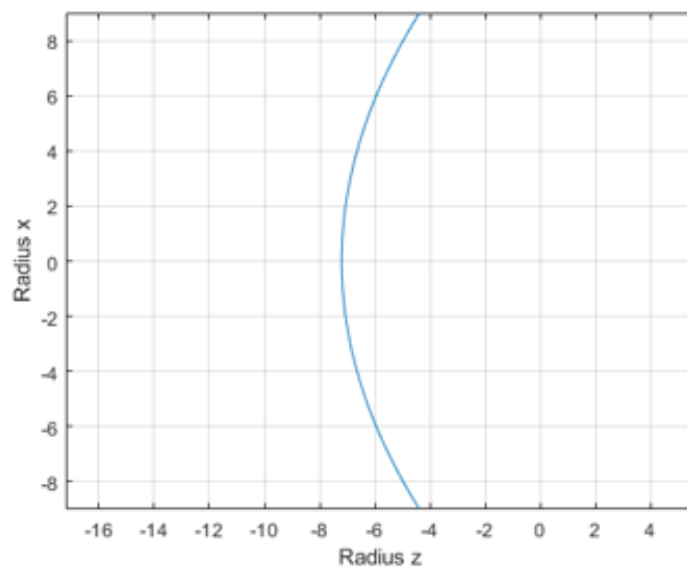


Figure 2.1: Geometrical representation of the parabolic reflector and the subtended angle  $\theta_0$ . from [2]

The design of parabolic reflectors is fundamentally grounded in geometric principles, aiming to achieve a constant phase front by ensuring equal path length characterized by the equation  $OP + PQ = 2f$  as shown in 2.1, where  $OP$  represents the distance from any point on the parabola to the focus, and  $PQ$  denotes the corresponding distance to the directrix, equating to twice the focal length. In the depicted scenario, the parabola is described by the radial distance  $r'$  at any given point  $P(x', y', z')$ , with  $PQ = r' \cos(\theta')$  and  $OP = r'$ . This relationship ensures a uniform phase front across the aperture, thereby creating the focus and directivity of the reflector. The equal path length condition can be restated as  $r'(1 + \cos(\theta')) = 2f$ , simplifying to  $r' = f \sec^2(\theta'/2)$ . This parameterization has been drawn in figure 2.2



(a) Parabolic reflector in 3D



(b) Parabolic reflector in 2D

Figure 2.2: Parabolic reflector in 2D and 3D

The unit vector normal to the reflector surface at any point is essential for characterizing the induced surface current density on the paraboloidal reflector's surface. It can be mathematically expressed as:

$$\hat{n} = -\frac{\partial f}{\partial r}\hat{a}_r + \frac{1}{r}\frac{\partial f}{\partial \theta}\hat{a}_\theta$$

where  $\hat{a}_r$  and  $\hat{a}_\theta$  are the unit vectors in the radial and polar directions and the surface function  $f(r, \theta)$  is defined as  $f(r, \theta) = r' - f \sec^2(\theta'/2)$ . A plot of the normal unit vector is shown in figure 2.3.

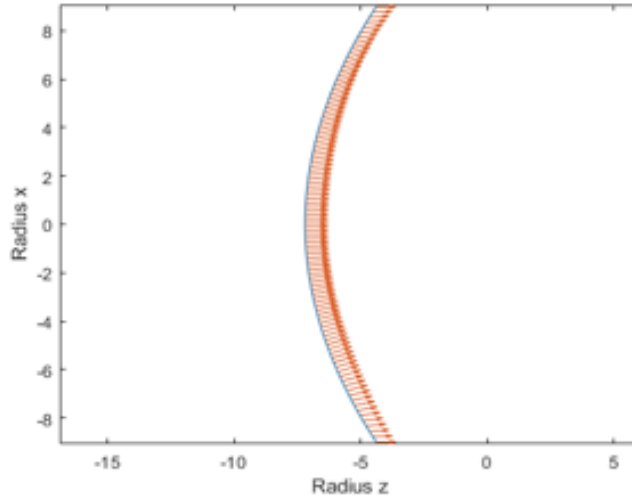


Figure 2.3: Normal vector of the reflector

The subtended angle  $\theta_0$  in relation to the  $f/d$  ratio is given by

$$\theta_0 = 2 \tan^{-1} \left( \frac{d}{4f} \right), \quad (2.1)$$

where  $d$  is the diameter of the reflector, and  $f$  is the focal length. The angle  $\theta_0$  is required for determining the efficient illumination of the reflector antenna.

### 2.2.1 Raised Cosine Feed Model

The Raised Cosine Feed Model is used to model the feed antennas radiation pattern. Proper choice of the parameters of this model minimize scattering losses at the rim edge of the parabolic reflector as seen in [16] and thereby increase the aperture efficiency. The

model gives the incident field as:

$$\vec{E}_f(\theta', \phi') = E_0 \cos^q \theta' \frac{e^{-jkr}}{r} (\hat{\theta} \cos \theta' \sin \phi' + \hat{\phi} \cos \phi')$$

where  $E_0$  represents the field amplitude in Volts,  $k$  is the wave number,  $r$  is the radius, and  $q$  defines the tapering factor that controls the directivity of the feed radiation pattern. The feed taper at the aperture edge,  $FT$ , and the spherical spreading loss,  $L_{sph}$ , are calculated as follows:

$$FT = -20 \log(\cos(\theta_0))$$

$$L_{sph} = 20 \log\left(\frac{r'}{r_0}\right) = 20 \log\left(1 + \frac{d^2}{16f^2}\right)$$

Edge illumination  $EI$  is subsequently determined by incorporating the edge taper  $ET$  and spherical spreading loss  $L_{sph}$ :

$$EI = -ET = -FT - L_{sph}$$

Solving for the tapering factor  $q$  yields:

$$q = \frac{\log\left(\frac{EI}{10^{20}} \left(1 + \frac{1}{16(F/D)^2}\right)\right)}{\log(\cos \theta_0)}$$

This equation facilitates the adjustment of the feed pattern to ensure optimal illumination of the parabolic reflector. As an example, the feed pattern depicted in figure 2.4 shows the y-polarized raised cosine feed model for a q-value of 1.4.

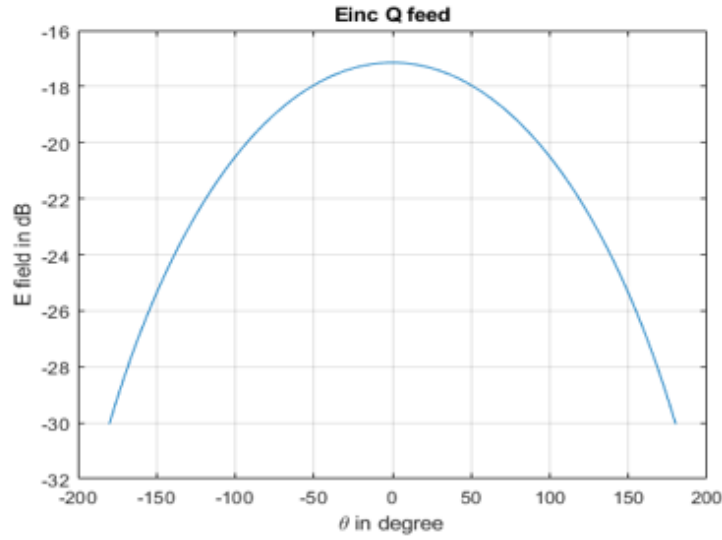


Figure 2.4: Example of Q feed ( $q=1.4$ )

## 2.2.2 Far-Zone Electric Field of a Parabolic Reflector

The far-zone electric field  $E_\theta$  for a parabolic reflector, which neglects the direct radiation, can be expressed as:

$$E_\theta = -\frac{j\omega\mu}{4\pi r} e^{-jkr} \iint_{S_1} \hat{a}_\theta \cdot \vec{J}_s e^{jk\vec{r}' \cdot \hat{a}_r} ds' \quad (2.2)$$

where  $\omega$  is the angular frequency,  $\mu$  is the permeability,  $r$  is the distance to the observation point,  $\vec{J}_s$  is the surface current density, and  $\hat{a}_\theta$  is the unit vector in the  $\theta$  direction. The double integral is evaluated over the reflector surface,  $S_1$ .

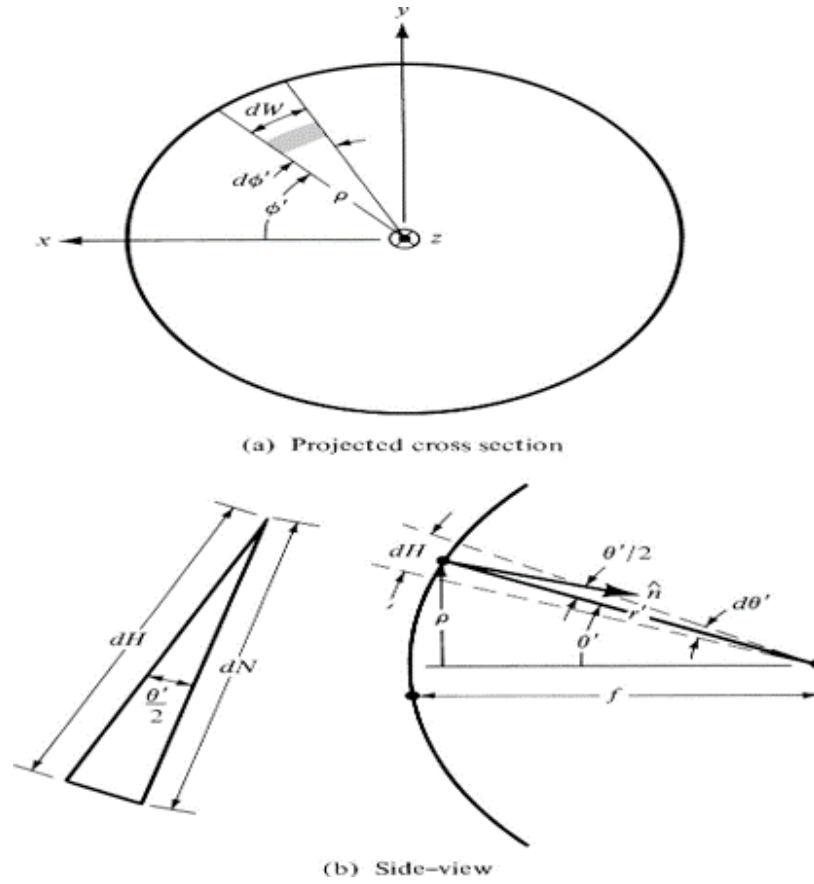


Figure 2.5: The far-field reflector geometry from [2]

Given the geometry of the parabolic reflector as shown in figure 2.5 , the differential surface element  $ds'$  can be described in terms of differential width  $dW$  and differential normal  $dN$ , leading to the relationship:

$$ds' = dW dN = r' \sin \theta' d\phi' \quad (2.3)$$

where  $dH = -\hat{a}'_r \cdot \hat{n} dN = r' d\theta'$  and simplifying  $dN$  gives us:

$$dN = r' \sec \left( \frac{\theta'}{2} \right) d\theta' \quad (2.4)$$

The expression for  $\hat{a}_\theta$  component of the far-field becomes:

$$E_\theta = -\frac{j\omega\mu}{4\pi r} e^{-jkr} \iint_{S_1} \hat{a}_\theta \cdot \vec{J}_s e^{jk\vec{r}' \cdot \hat{a}'_r} \sin \theta' \sec \left( \frac{\theta'}{2} \right) d\theta' d\phi' \quad (2.5)$$

This equation models the  $\hat{a}_\theta$  component of the far-zone field, taking into consideration the paraboloidal shape of the reflector's surface. The  $E_\phi$  represents the  $\hat{a}_\phi$  component of the electric field and is similarly expressed as:

$$E_\phi = -\frac{j\omega\mu}{4\pi r} e^{-jkr} \iint_{S_1} \hat{a}'_\phi \cdot \vec{J}_s e^{jk\vec{r}' \cdot \hat{a}'_r} \sin \theta' \sec \left( \frac{\theta'}{2} \right) d\theta' d\phi' \quad (2.6)$$

The total scattered field is then found as [5]:

$$\vec{E}_s(r, \theta, \phi) = -j\omega\mu \frac{e^{-jkr}}{4\pi r} \int_{\theta_0}^{\theta'} \int_0^{2\pi} \vec{J}_s(\vec{r}'_i) \times e^{jkri(\sin \theta \cos(\phi' - \phi) + \cos \theta' \cos \theta)} \times r_i^2 \sin \theta' \sec^2 \left( \frac{\theta'}{2} \right) d\theta' d\phi'$$

Ludwig's III definition is applied to determine the co-polarized and cross-polarized components of the far-field pattern  $\vec{E}_{co,cr}(\theta, \phi)$ , given by:

$$\vec{E}_{co,cr}(\theta, \phi) = \mathbf{T} \cdot \vec{E}_{sc}$$

Where the Ludwig's III dyad,  $\mathbf{T}$ , is defined as

$$\mathbf{T} = \begin{pmatrix} 0 & 0 & 0 \\ 0 & \cos \phi & \sin \phi \\ 0 & \sin \phi & -\cos \phi \end{pmatrix}$$

for  $x$ -polarized feeds, and

$$\mathbf{T} = \begin{pmatrix} 0 & 0 & 0 \\ 0 & \sin \phi & \cos \phi \\ 0 & \cos \phi & -\sin \phi \end{pmatrix}$$

for  $y$ -polarized feeds. Note the negative sign in the second column of these matrices with respect to the definition in [20] is due to the reversal in the direction of the  $\hat{\theta}$  unit vector in the lower hemisphere ( $x, y, z < 0$ ) from figure 2.1, where the radiation pattern is being calculated.

The directivity patterns for both co-polarized and cross-polarized components can be determined from the radiated power  $P_{rad}$ , which is approximated the power of the raised cosine feed that is captured by the reflector as:

$$P_{rad} = \frac{E_0^2 2\pi}{2\eta_0(2q+1)} (1 - \cos^{2q+1} \theta_0) \quad (2.7)$$

The co-polarized directivity  $D_{co}$  is then found from:

$$D_{co} = \frac{U_{co}}{U_{avg}} = \frac{4\pi r^2 |\vec{E}_{co}|^2}{2\eta_0 P_{rad}} \quad (2.8)$$

where  $U_{co}$  is the radiation intensity for the co-polarized component and  $U_{avg}$  is the average radiation intensity.

Similarly, the cross-polarized directivity  $D_{cr}$  is derived from the ratio of the radiation intensity for the cross-polarized component  $U_{cr}$  to the average radiation intensity  $U_{avg}$ , and it can be calculated as follows:

$$D_{cr} = \frac{U_{cr}}{U_{avg}} = \frac{4\pi r^2 |\vec{E}_{cr}|^2}{2\eta_0 P_{rad}} \quad (2.9)$$

In the following example, the raised cosine feed model is used to illuminate a parabolic reflector with the following specifications:

- Focal length ( $F$ ) is 0.4 times the diameter ( $D$ ) of the reflector.
- The diameter ( $D$ ) of the reflector is 18 meters.
- Edge illumination ( $EI$ ) is set to -10 dB.

*The edge illumination ( $EI$ ) is set to -10 dB as this value ensures a good balance between spillover and under-illumination in axisymmetric prime focus fed parabolic reflector antennas.*

. A y-polarized Raised Cosine Feed Model calculated from the above specifications is employed. The co-polarized directivity pattern is plotted in figure 2.6

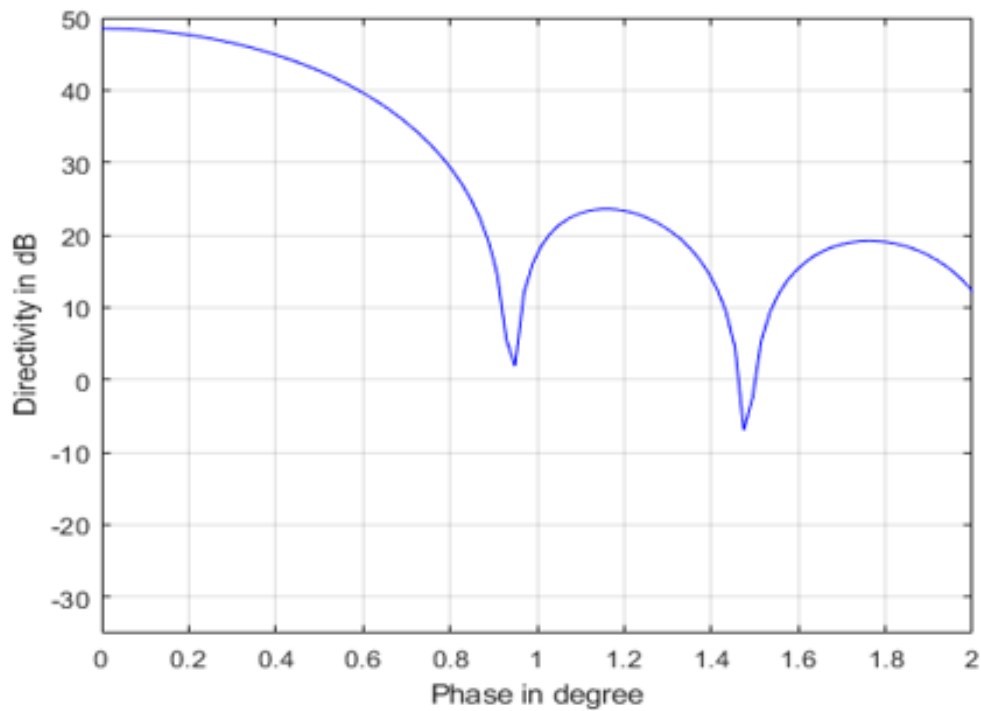


Figure 2.6: The co-polarized and cross-polarized directivity patterns

This pattern agrees with that in reference [5] and [7].

## 2.3 Reflectarray Antenna Functionality

The parabolic reflector exhibits a constant phase upon reflection as seen in [12]. This property leads to the design of a reflectarray based on similar path length equality principles. By tuning the local reflection coefficient phase angle, the electrical path lengths shown in figure 2.7 can be made equal.

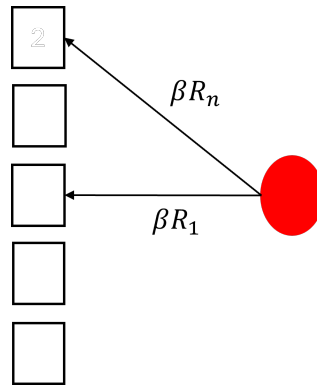


Figure 2.7: The design principle of a reflectarray

This principle mirrors the operation principles of parabolic reflectors, which maintain a uniform phase distribution across the reflected wavefront, thereby achieving a collimated beam for maximal directivity.

The unit cells are designed such that the angle of the local reflection coefficient,  $\angle\Gamma$ , compensates for the electrical path length difference shown in figure 2.7. The books [13] and [22] can be referenced for more background in reflectarrays.

Each element is a miniaturized patch or dipole, functioning as a discrete phase shifter. By tuning the length, shape, or the dielectric properties of these elements, one can dictate the phase shift each element imparts to the incident wave. This is critical for modifying the antenna's radiation pattern, bandwidth, and polarization characteristics, making reflectarrays a versatile tool in antenna designs.

## 2.4 Design Principles of Wide-band Reflectarray Elements

One of the common elements for the design of a reflectarray is a patch antenna. Patch antennas are widely used in various applications due to their compact size and ease of fabrication. However, a common limitation of conventional patch antennas is their lack of wide-band capabilities. This means that they may not perform optimally across a broad range of frequencies, limiting their versatility in certain applications.

To address this limitation and achieve wide-band capabilities, researchers have explored alternative antenna designs. One such design is the E-shaped patch antenna, which has garnered significant interest in recent years. The geometry of the E-shaped patch antenna offers improved bandwidth performance over traditional patch antennas.

The E-shaped patch antenna was initially studied as a potential solution to the narrow-band limitations of conventional patch antennas from [19] and [25]. One of the requirements of the research was to explore new antenna configurations that could achieve wide-band operation while maintaining the ease of fabrication associated with patch antennas.

The E-shaped patch antenna from [25] is shown in figure 2.8. The E-shaped patch utilizes a foam substrate to closely emulate the properties of air with the parameters summarized in the table 2.1.

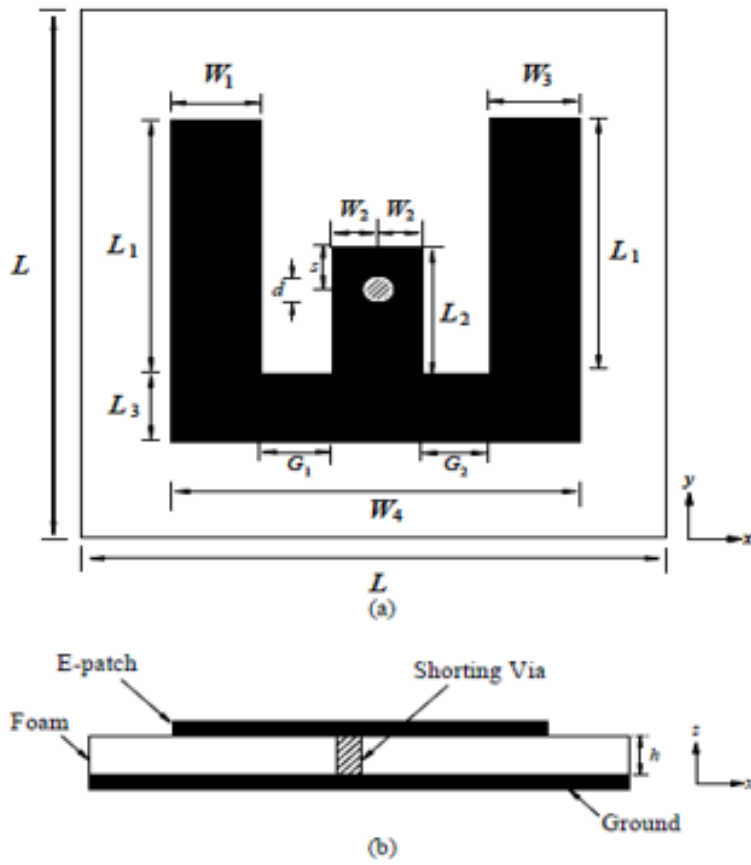


Fig. 1. (a) Top view. (b) Side view of the proposed E-patch unit element.

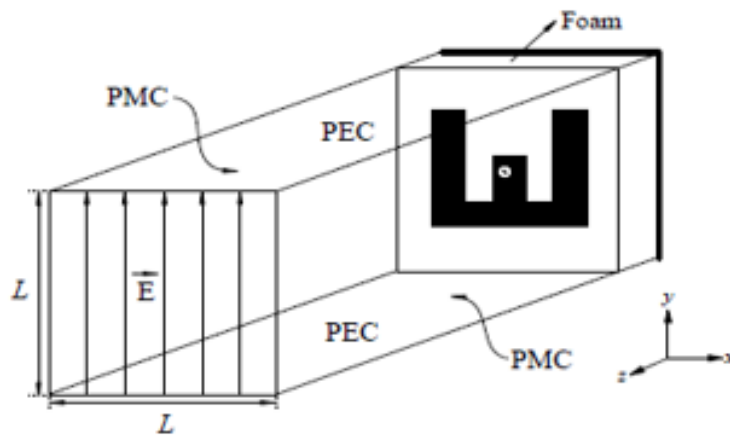


Fig. 2. Simulation setting for the proposed unit element inside a Floquet cell.

Figure 2.8: An E-shaped patch antenna design with marked dimensions from [25].

Table 2.1: E-shaped Patch Antenna Design Parameters

Parameter	Value (mm)
Arm Widths ( $W1, W3$ )	3
Gap ( $G1, G2$ )	3
Arm Width ( $W2$ )	2
Length ( $L3$ )	3
Length ( $L2$ )	7
Spacing ( $s$ )	3
Depth ( $d$ )	1

As observed in figure 2.9, the angle of the reflection coefficient is plotted against the arm length parameter  $L_1$  of the E-shaped patch.

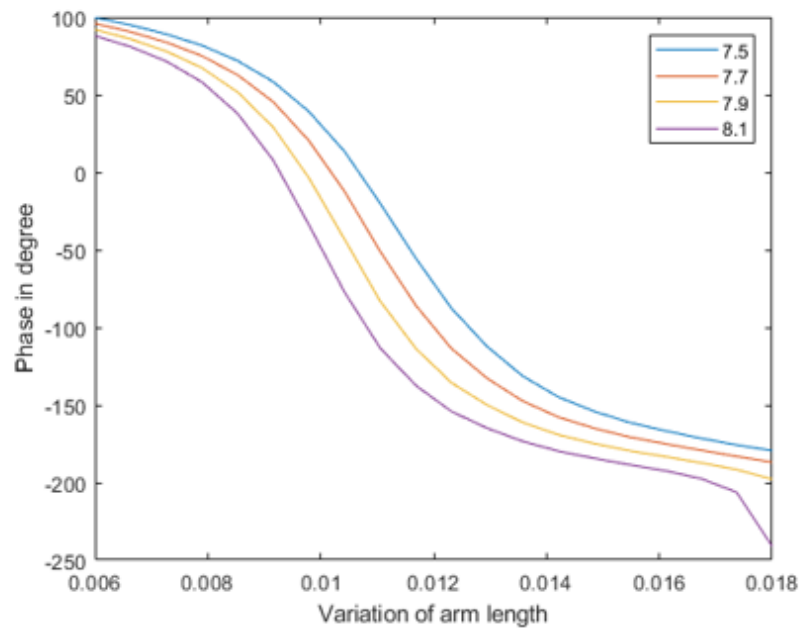


Figure 2.9: Phase response of the E-shaped patch antenna corresponding to variations in arm length.

As can be seen in the figure, the phase curves are nearly parallel indicating wideband behaviour. However, the E-shaped patch antenna is not dual-linearly polarized and hence cannot be used in our intended application. To achieve dual-linear polarization and wideband

response, we introduce a symmetric slot loaded unit cell in chapter 3. .

## 2.5 Dual-Band and Dual-Polarized Performance Objectives

To address the dual-polarization requirement, the unit cell is designed to respond equally to both horizontal and vertical polarizations. In this thesis, the simulations are presented for x-polarized feeds. However, because the reflectarray elements are symmetric, y-polarized feeds are expected to produce similar outcomes.

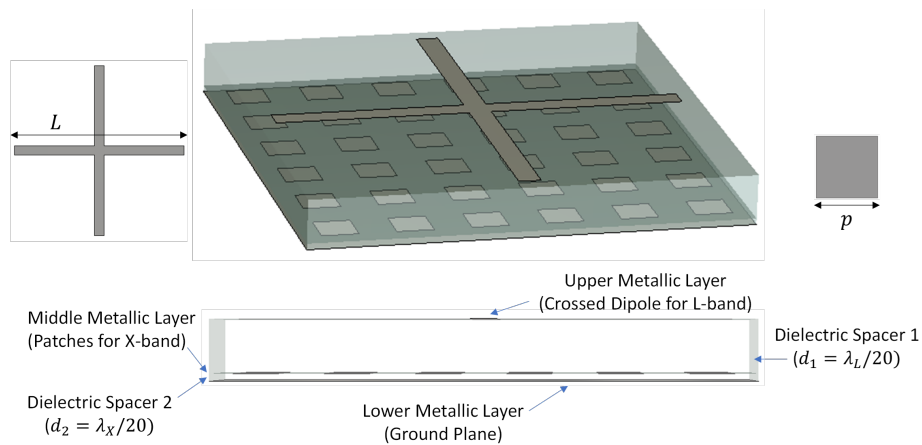


Figure 2.10: An antenna design example configured for dual-band and dual-polarized operation.

An example of a multilayer dual band reflectarray design is shown in figure 2.10. The figure shows an X-band layer of patches that should work over the frequency range of the Starlink's X band, from 10.7 to 12.7 GHz. The integration of a superstrate onto the X-band layer supports elements which operate over the Iridium's L-band frequency range around 1.62 GHz. The design shown does not provide the required bandwidth in the X-band, and hence we will replace the square patches with a wideband element. The new wideband element is described in chapter 3.

## Implementation of the Raised Cosine Feed Model

To feed the reflectarray, we adopt the Raised Cosine feed model as was introduced in section 2.2.1.

In all simulation results presented henceforth, the electric field  $\vec{E}_f$  is used to define the incident field. The amplitude of the electric field is denoted by  $E_0$  in Volts, and the dependence of the field on the angle  $\theta'$  is governed by the term  $\cos^q(\theta')$ , where  $q$  is the shaping factor. The field is x-polarized.

$$\vec{E}_f(\theta', \phi') = E_0 \cos^q(\theta') \frac{e^{-jkr}}{r} (\hat{\theta} \cos \theta' - \hat{\phi} \sin \phi')$$

The feed is located at a distance of  $D/2$  where  $D$  is the maximum dimension of the reflectarray. The edge illumination (EI) is set to -10 dB. The value of  $q$  can be calculated

$$q = \log_{10} \left( \frac{0.1}{2 \times \log_{10}(\cos(45))} \right) = 3.3219$$

and the corresponding incident field is shown in figure 2.11.

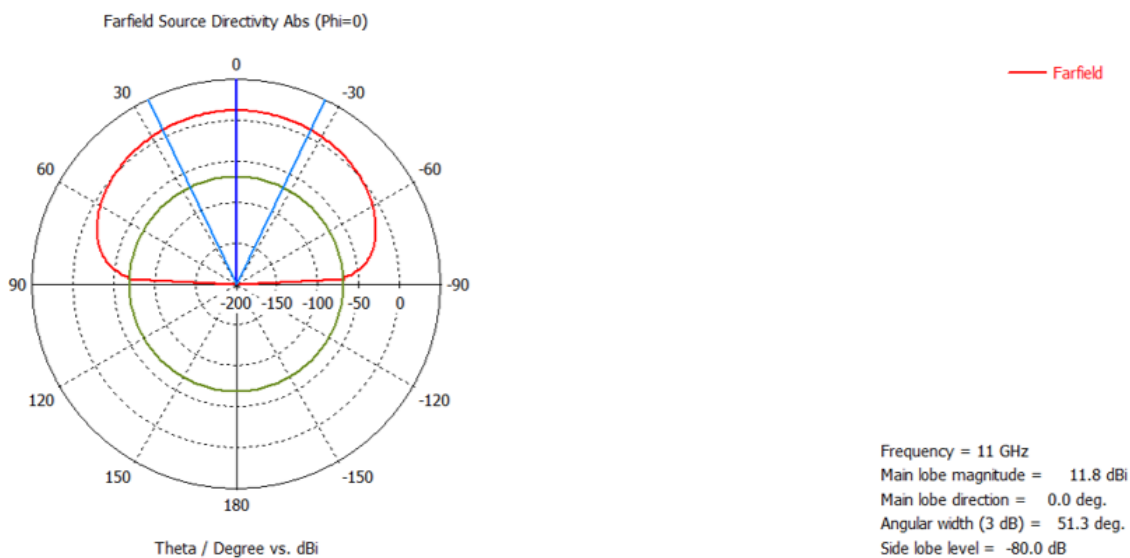


Figure 2.11: Raised cosine  $q$  feed model scattering at 11 GHz

# Chapter 3

## Unit Cell Design and Reflectarray

### Design at X-Band

#### 3.1 Unit Cell Design at X-Band

In electromagnetics and microwave engineering, unit cells can be visualized as small pieces of a periodic structure that are combined to make a larger aperture. In this thesis, a wide-band unit cell in the X-band is desired. The angle of the reflection coefficient can be plotted against a geometrical variable parameterizing the unit's cell's geometry. This curve is typically called an S-curve. When these S-curves are nearly linear and only exhibit a vertical shift with frequency, the unit cell can be said to be wideband as explained in [30]. *Thus, the metric for assessing wide-band behavior is the linearity of the calculated S-curves and that they are approximately parallel to one another at different frequencies.*

Recent studies have explored the concept of varying slot geometries in unit cell designs [30]. This chapter looks at designing a slot loaded dual-polarized unit cell that can work well over the wide range of frequencies from 10.7 to 12.7 GHz. A reflectarray utilizing this unit cell geometry is then designed and simulated in CST Microwave Studio (MWS).

### 3.1.1 Unit Cell Geometry

The unit cell with L-shaped slots was selected due to the observed linearity of the S-curve, as illustrated in figure 3.4. As eluded to, this linearity suggests wide-band capability making it a suitable choice for the intended application.

The unit cell, as depicted in figure 3.1, is characterized by a geometry taken from [29]. It is enclosed by unit cell periodic boundaries, indicating its integration into a larger, infinitely repeating array.

The unit cell design incorporates slot oriented along the four edges of the unit cell. This configuration lead to a dual-polarized response. As the length  $L$  of the slots are varied, the reflection phase can be tuned over nearly 360 degrees as referenced from [29], [27],[24],[9],[11]and [10].

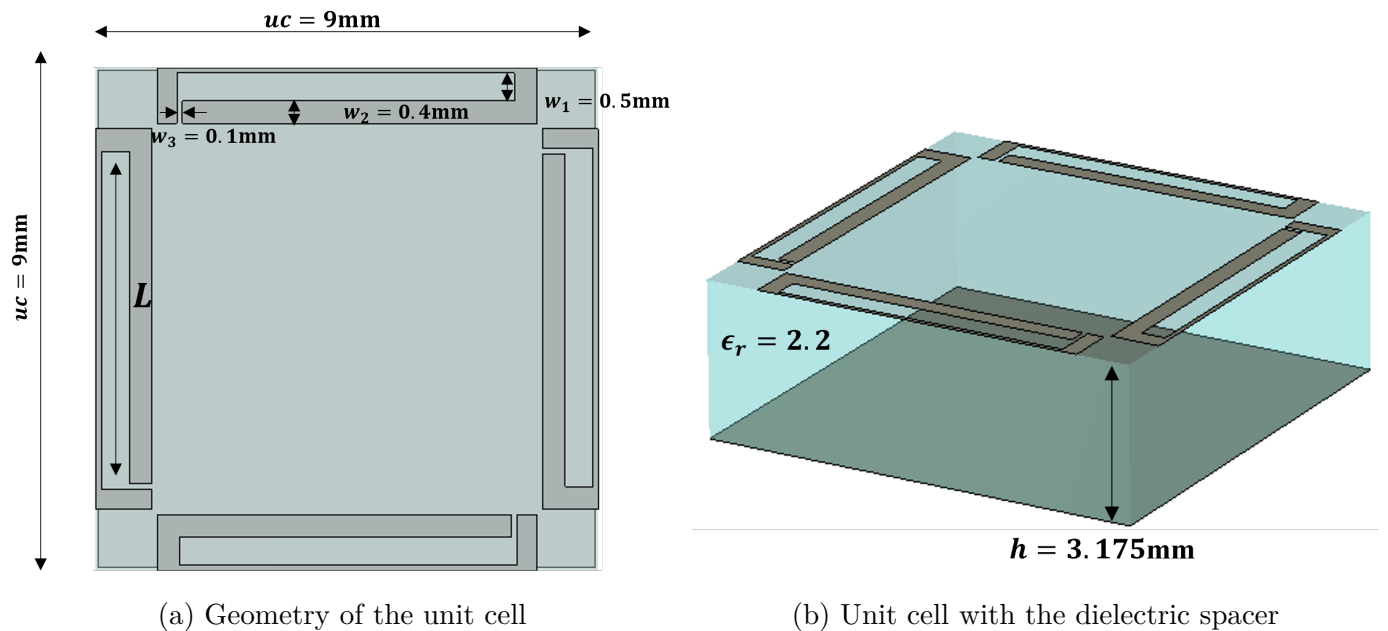


Figure 3.1: Unit cell geometry

The figure gives the dimensions of the unit cell as  $9 \times 9$  mm. The other parameters of the L-slot patches denotes widths  $w_1$ ,  $w_2$ , and  $w_3$  as well as the length  $L$ , with  $w_1$  being

0.5 mm  $w_2$  being 0.4 mm and  $w_3$  being 0.1 mm, whereas  $L$  mm is to be determined. These are summarized in the table 3.1.

Table 3.1: Geometric Parameters of the Unit Cell

Parameter	Value (mm)
Unit Cell Dimension	9
Width $w_1$	0.5
Width $w_2$	0.4
Width $w_3$	0.1
Height of Substrate	3.175

### 3.1.2 Unit Cell Simulation Setup

The unit cell was modeled in CST Microwave Studio with simulations employing the *unit cell boundary condition* and excited at normal incidence with *Floquet ports*. The unit cell boundary condition and the simulation setup used for the analysis are shown respectively in figures 3.2 and 3.3.

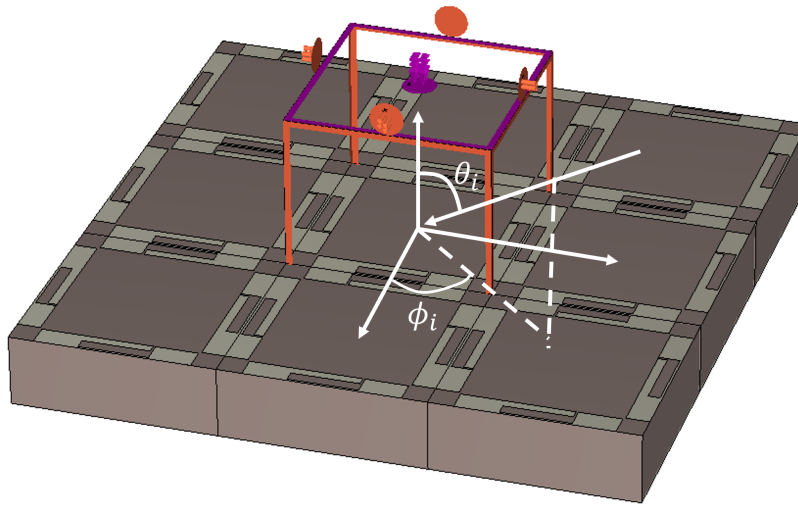


Figure 3.2: Unit cell with periodic boundaries

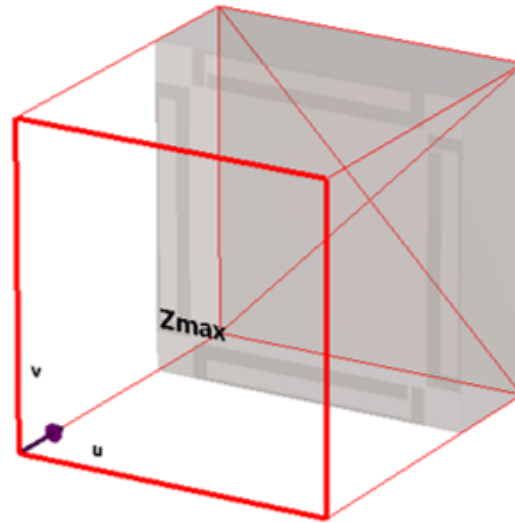


Figure 3.3: Unit cell simulation setup

In the analysis of the unit cell's performance, the following aspects are observed:

- The variation of the reflection phase with respect to the slot length at 11 GHz.
- The influence of oblique incident angles on the reflection phase.
- The relationship between the slot length and the reflection phase examined across a range of frequencies from 10 to 13 GHz.

### 3.1.3 Unit Cell Simulation Results and Discussions

Key findings indicate that by adjusting the slot length, a linear range of reflection phase of  $350^\circ$  at 11 GHz was achieved. The unit cell's performance was tested under normal incidence, showing linearity in the reflection phase across the length of the slots shown in figure 3.4, for horizontal polarization. Similar results are obtained for vertical polarization.

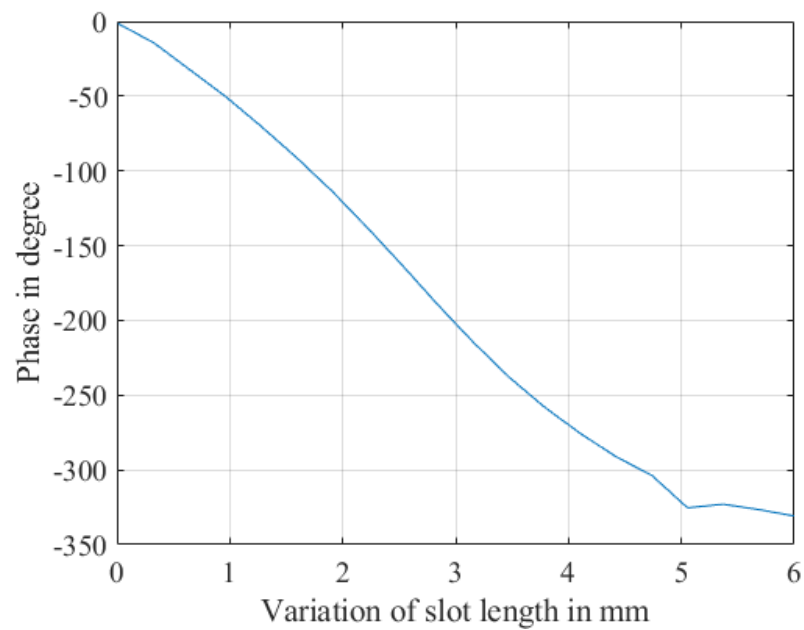


Figure 3.4: S-curve at 11 GHz

### Angle of Incidence Effect and Bandwidth Performance

The analysis was extended to study the effect of oblique incidence angles on the unit cell's performance. Reflection phase characteristics were maintained up to a  $40^\circ$  incidence angle as shown in the corresponding figure 3.5, indicating that the design is robust up until that value of incidence angle.

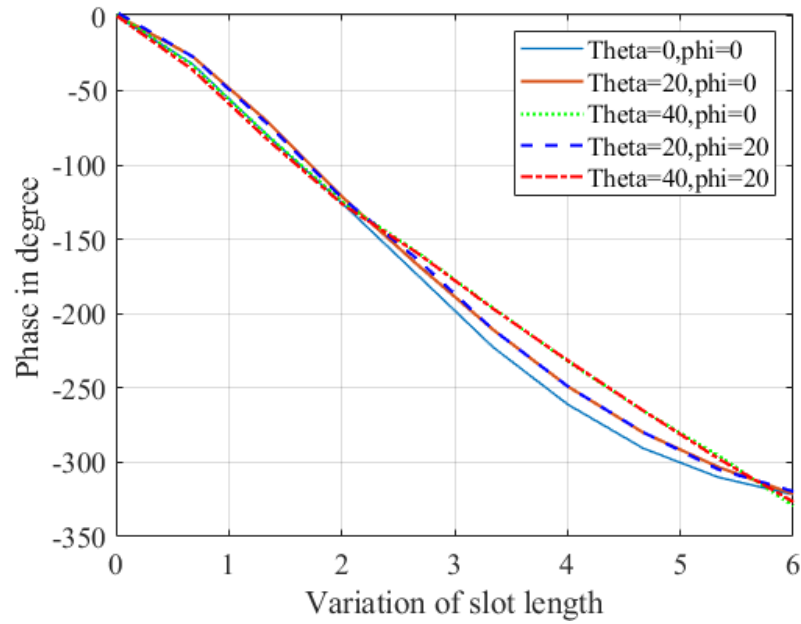


Figure 3.5: S-curves at various incident angles

Thus, the reflectarrays in this thesis can be designed by considering the unit cell's S-curve obtained at normal incidence only.

Graphical analysis through S-curve plots across various frequencies in figure 3.6 reveals that the S-curves are nearly parallel with frequency. This observation suggests that the unit cell is capable of operating over a wide frequency band, confirming the efficacy of the sliding slot design.

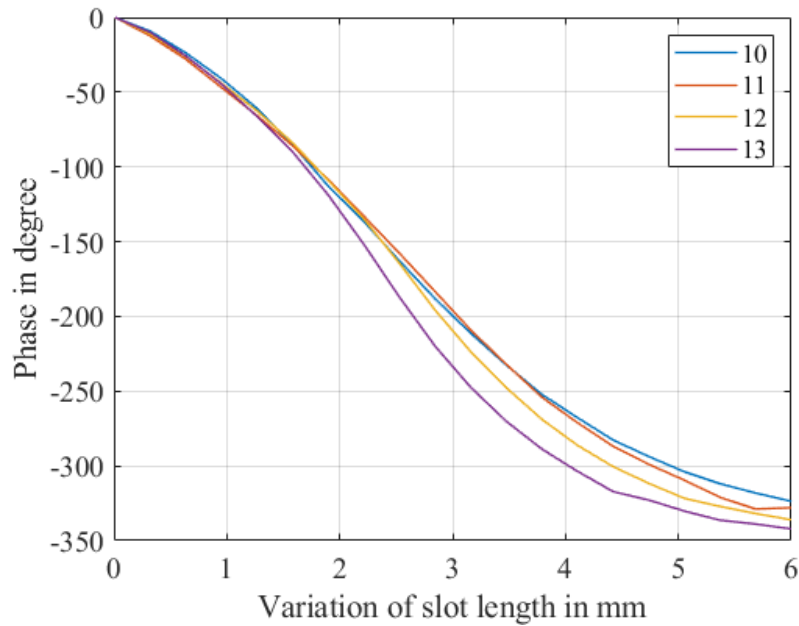


Figure 3.6: S-curves at various frequencies

The results obtained for the sliding slot unit cell supports its potential for the attainment of a wide-band reflectarray design at the Starlink frequency band.

## 3.2 Reflectarray Design at X-Band

Through the simulation of the unit cell, the reflection coefficient phase against the geometrical parameter  $L$  is obtained. This data can be used to map a particular unit cell geometry to each location in the reflectarray by providing a local reflection coefficient that compensates for the differential path length to that unit cell. We describe how to translate the data in the S-curve and the geometry of the reflectarray into the local unit cell geometries next.

### 3.2.1 Design of the Reflectarray

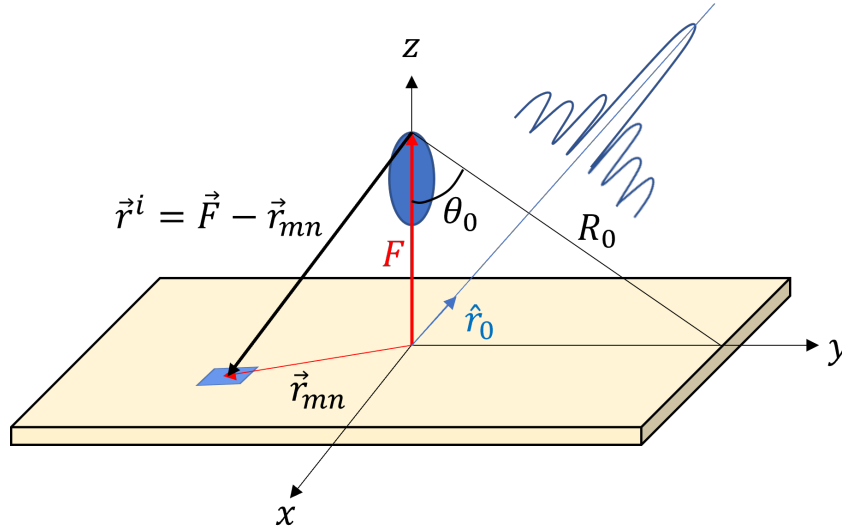


Figure 3.7: Reflectarray design geometry

The variables  $m$  and  $n$  represent the indices of the rows and columns, respectively, in the reflectarray configuration. For the examples of this section, both  $m$  and  $n$  are assigned a value of 15, constituting an array with a total of 225 unit cells. The overall dimensions of the array are  $135 \times 135 \text{ mm}^2$ . This is equivalent to  $5\lambda$  when the frequency is considered at 11 GHz.

The vector  $\vec{r}_{mn}$  is defined as the position vector to the center of each unit cell with respect to the coordinate origin located at the center of the reflectarray. This vector is calculated as  $m\hat{a}_x + n\hat{a}_y$ , where  $\hat{a}_x$  and  $\hat{a}_y$  are the lattice vectors in the x and y directions, respectively, and is depicted in figure 3.7.

The vector  $\vec{F}$  represents the position vector to the feed point from the center of the reflectarray. In this model,  $|F|$  is set to half the dimension of the reflectarray antenna, which equates to 67.5 mm.

Applying principles of vector algebra, the vector  $\vec{r}_i$  can be obtained by forming the

difference  $\vec{r}_i = \vec{r}_{mn} - \vec{F}$ . The phase  $\phi_{mn}$  of the incident field at each patch is then a function of the magnitude of the vector  $\vec{r}_{mn}$ , as  $\phi_{mn} = k_0 |\vec{r}_i|$ , where  $k_0$  is the free space wave number. In the construction of the reflectarray antenna, the desired value of  $L$  is determined by conjugating the phase  $\phi_{mn}$  and finding this value in the S-curve vs.  $L$  at 11GHz. The desired  $\phi_{mn}$  to form a broadside beam are delineated in Appendix A.1.

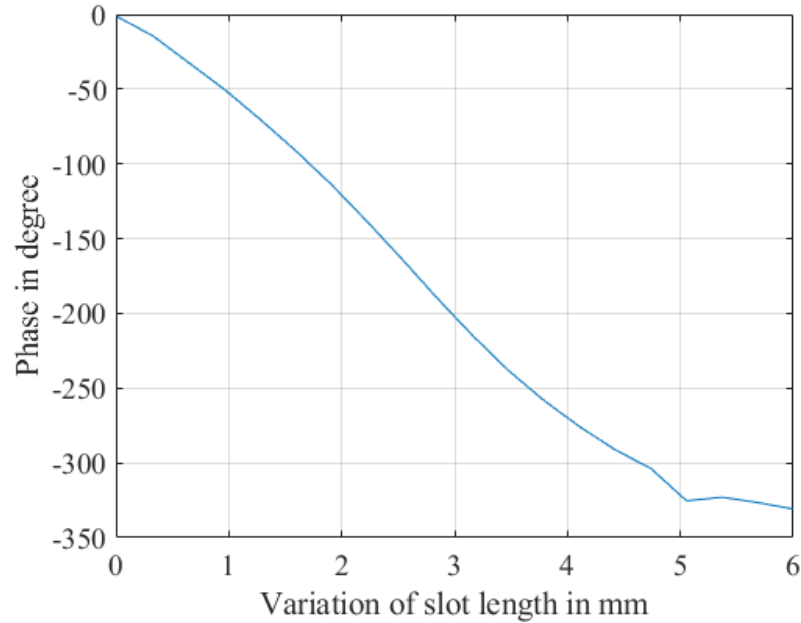


Figure 3.8: S-curve at 11 GHz

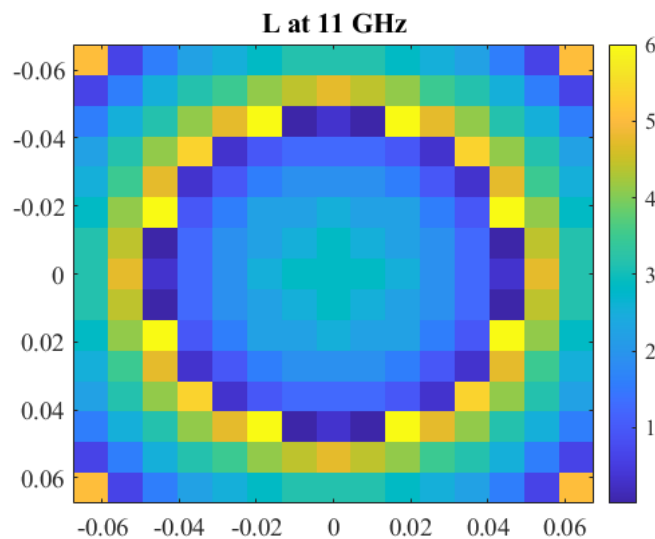


Figure 3.9: Analytical reflectarray construction at 11 GHz

The resultant analytical geometry is illustrated in figure 3.9. This figure in conjunction with the unit cell geometry in figure 3.1 allows for the construction of the reflectarray antenna utilizing the values of the slot length,  $L$  in millimeters (mm), depicted in the colorbar. Note, the dimensions along the x and y directions of figure 3.9 are in meters (m).

### 3.2.2 Reflectarray Simulation

The reflectarray is designed and simulated within the CST Microwave Studio environment. The reflectarray consisting of the slot loaded unit cells is drawn using the macro facilities provided by the software based on the extrapolated values from figure 3.9 .

Maintaining the same geometric structure, the reflectarray shown in figure 3.10 is simulated across various frequencies to observe and study the behavior of the far fields.

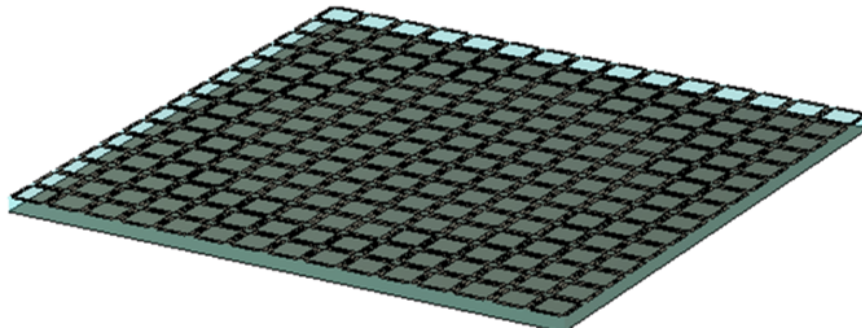


Figure 3.10: Reflectarray at X-band and simulation setup

### Result Analysis of Reflectarray Antenna

After setting everything up, the *Integral Equations Solver* in CST was chosen to obtain co-polarized far fields. The geometric configuration of the reflectarray remains unchanged during simulations at different frequencies. The plot in figure 3.11 below shows the co-polarized far field at the indicated frequencies 10.7 GHz, 11 GHz and 12.7 GHz.

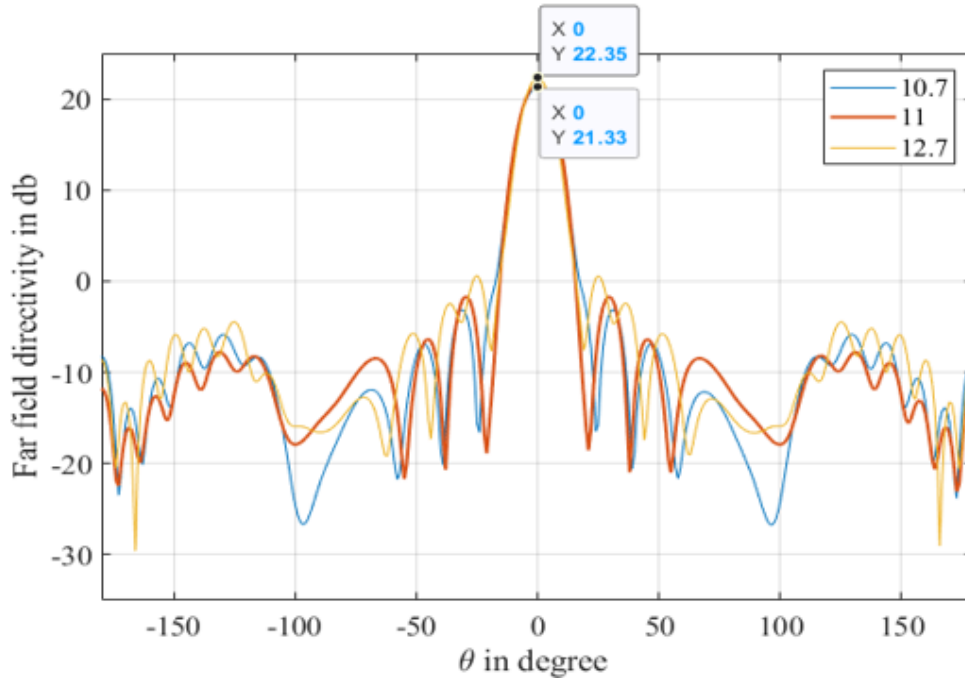


Figure 3.11: Co-polarized far fields at X-band for various frequencies

### Frequency Response and Bandwidth Analysis

The far fields at 10.7 GHz, 11 GHz and 12.7 GHz show collimation and realize a broad 1-dB directivity bandwidth of 17.1%.

Note, the 1-dB directivity bandwidth is calculated as  $\frac{f_{upper} - f_{lower}}{f_{center}} \times 100$ , where  $f_{upper}$  and  $f_{lower}$  correspond to the frequencies at which the directivity drops by 1dB with respect to the main beam peak value.

*Summarizing, far-field patterns are plotted to assess the reflectarray antenna's performance across the X-band frequency spectrum. The collimation of fields across the frequency range confirms the design's wide bandwidth.*

### 3.3 Impact of Superstrate on X-Band Layer Performance

The effect of a superstrate layer on the slot loaded unit cell is studied next. The superstrate is necessary to support the L-band elements required for the dual band operation.

However, the integration of a superstrate above the X-band layer brings about modifications to the slot loaded unit cell's performance characteristics. It is essential henceforth that the superstrate thickness is optimized such that it is capable of maintaining the wide-band performance at the X band .

#### 3.3.1 Unit Cell and Reflectarray Design with Superstrate

The unit cell, coupled with a superstrate having the same material parameters as the substrate, is redesigned to maintain its performance across the X-band. The new unit cell is shown in figure 3.12.

The thickness of the optimized superstrate is  $\frac{\lambda_1}{10}$ , where  $\lambda_1$  represents the wavelength at L band (1.62 GHz), as determined through parametric studies in CST MWS. The chosen permittivity,  $\epsilon_r = 2.2$ , also ensures minimal disruption to the material's parameters.

This unit cell's operation is also studied at 11 GHz and has periodic boundaries, with excitation provided by Floquet Ports at normal incidence as seen in section 3.1.2. The parameters of the unit cell is summarized in the table 3.2

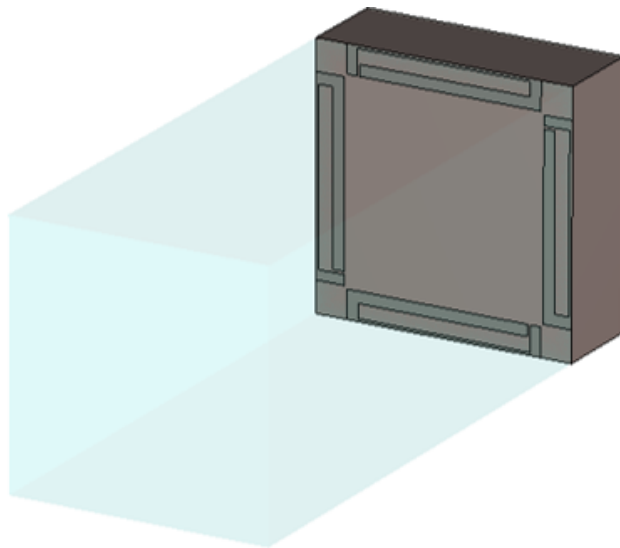


Figure 3.12: The unit cell with superstrate

Table 3.2: Geometric Parameters of the Unit Cell with superstrate

Parameter	Value (mm)
Unit Cell Dimension	9
Width $w_1$	0.5
Width $w_2$	0.4
Width $w_3$	0.1
Height of Substrate	3.175
Height of Superstrate	18.185

The S-curves seen in figure 3.13 at different frequencies are almost parallel. This response is thus indicative of the unit cell's wide-band response in the design frequencies ranging from 10.7 to 12.7 GHz.

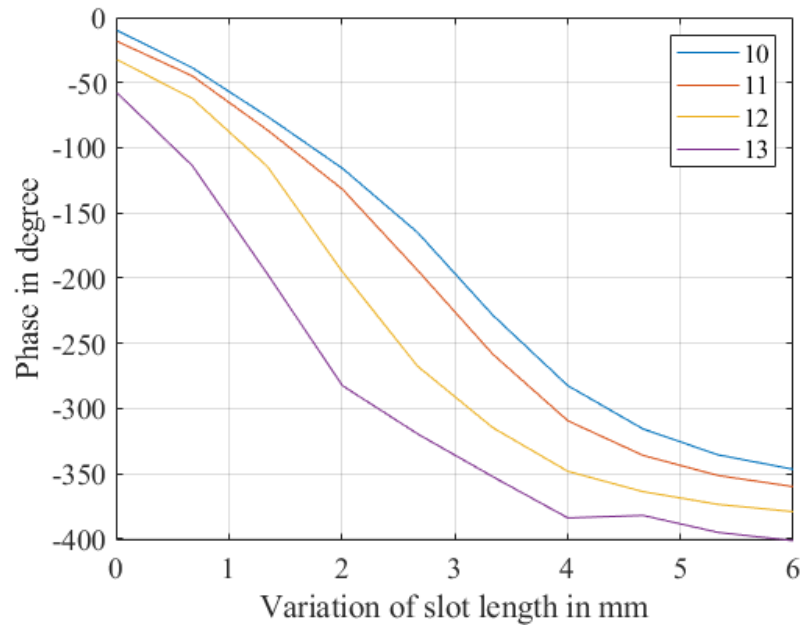


Figure 3.13: S-curves of the unit cell with superstrate

As discussed in Subsection 3.2.1, the desired value of  $L$  is derived by conjugating the phase  $\phi_{mn}$ . The final layout is shown in 3.14 with the scale for the slot length  $L$  in the colorbar in units of millimeters (mm) and the dimensions along the x and y directions in units of meters (m).

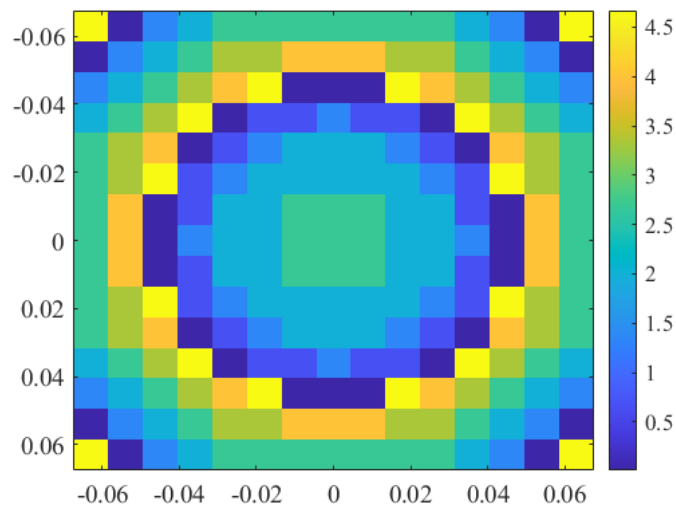


Figure 3.14: Analytical reflectarray construction with superstrate at 11 GHz

### 3.3.2 Far-field Performance of the Reflectarray with Superstrate

The reflectarray is drawn in CST MWS, utilizing the calculated values for slot length,  $L$ , shown in figure 3.14 using the software's macro environment. The raised cosine feed model is employed as the incident field. The reflectarray CAD model is shown in figure 3.15.

Far-field patterns are plotted to assess the antenna's performance at the frequencies 10.7 GHz, 11 GHz and 12. GHz as seen in figure 3.16. The same geometric configuration for the reflectarray is maintained for all the frequencies.

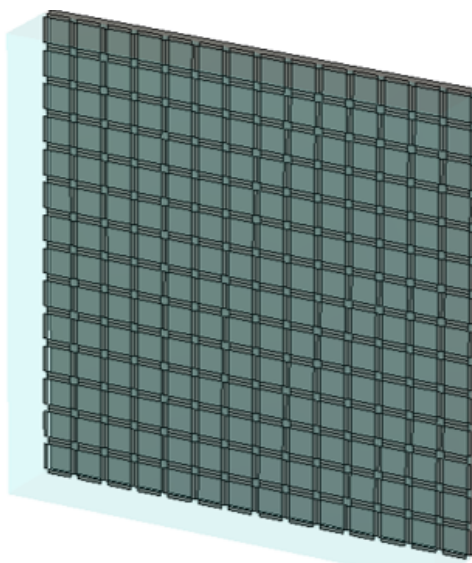


Figure 3.15: Reflectarray with superstrate

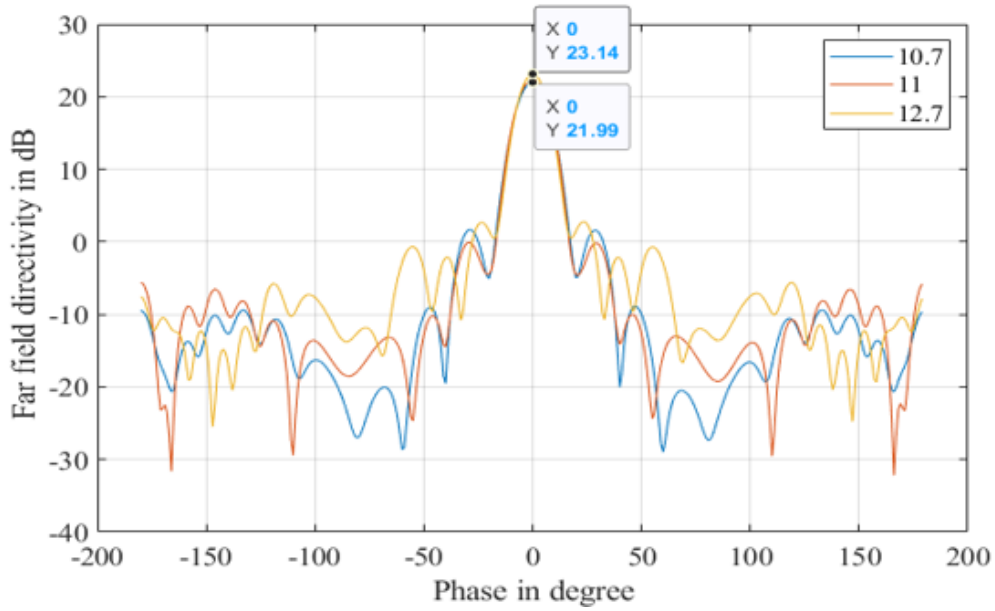


Figure 3.16: Co-polarized fields at X-band with superstrate

The collimation of the fields across the frequencies also realizes a 1-dB directivity bandwidth confirming the design's wide bandwidth. The calculated bandwidth requirement of 17.1% for the specified frequency range remains unaffected. Given the established wide-band capabilities of the X-band reflectarray with the optimally thickened superstrate in figure 3.16, the next design phase detailed in chapter 4 involves designing the L-band unit cell.

# Chapter 4

## Unit Cell and Reflectarray Design at L-Band

### 4.1 L-Band Unit Cell

The unit cell design for the L-band employs a cross dipole antenna. The reasons for choosing this design has been summarized in the points below:

- Dual-polarized radiation: Cross dipole antennas can transmit or receive signals with both horizontal and vertical polarizations.
- Thin profile: Dipoles are inherently thin advantageous for dual-band models, as it minimizes blockage for other frequency bands.
- Simple structure: With only two identical dipoles oriented perpendicular to each other, cross dipole antennas are easy to design.

A preliminary study of the cross dipole antenna reflectarray was done in [8] to gain insights of its characteristics and performance. The chapter focuses on designing the unit cell and henceforth the reflectarray at the Iridium's frequency range around 1.62 GHz.

#### 4.1.1 Design Considerations for L-Band Operation

In the design of the L-Band unit cell, the cross dipole antenna is placed on the superstrate layer. The substrate thickness beneath the superstrate mirrors the dimensions of the

X-band unit cell as detailed in the subsection 3.3.1, ensuring future integration within the design's overall architecture. Additionally, the entire assembly is grounded using a Perfect Electric Conductor(PEC) ground plane.

The dipoles are rotated by  $45^\circ$  since when subsequently integrated into the X-band layer, it was found that this angle minimizes blockage for at the X-band frequencies.

The material chosen for the superstrate has a thickness,  $\frac{\lambda_1}{10}$  as already mentioned has a permittivity ( $\epsilon_r$ ) of 2.2 and is considered lossless. At L band the unit cell dimension is chosen as  $0.7\lambda$ , where

$$0.7\lambda = 0.7 \times \frac{3.00}{1.62} \times 10^2 \text{ mm} \approx 129 \text{ mm}$$

The final design of the L band unit cell is shown in figure 4.1.

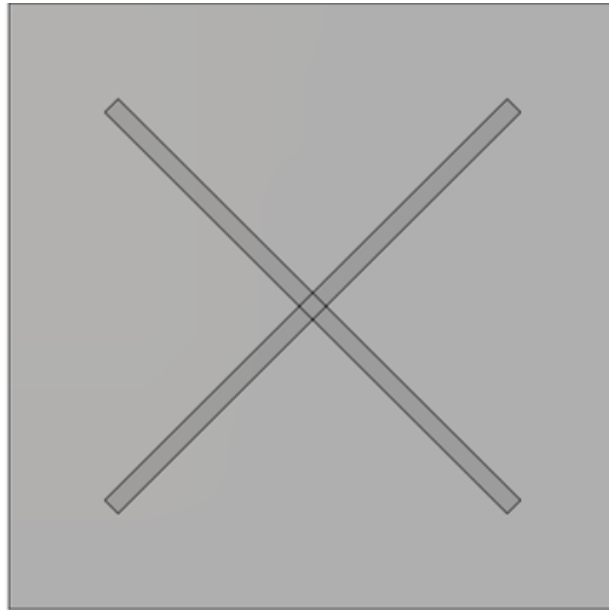


Figure 4.1: L-band (Cross Dipole) unit cell

The parameters of the same are summarized in the table 4.1.

Table 4.1: Geometric Parameters of the L-Band Unit Cell

Parameter	Value (mm)
Unit Cell Dimension	129
Height of Substrate	3.175
Height of Superstrate	18.185

### 4.1.2 Phase Range Analysis of the Cross Dipole at 1.62 GHz

An important aspect of the L-band unit cell design is the analysis of the S-curve at 1.62 GHz. The S-curve depicted in figure 4.2 gives a graphical representation of the phase of the reflection coefficient as a function of the varying geometric parameter, namely, the length of the cross dipole antenna arm. It was found that the maximum tunable phase range was  $330^\circ$ . *This phase range is important for the successful design of the reflectarray as this allows the reflectarray to collimate effectively.*

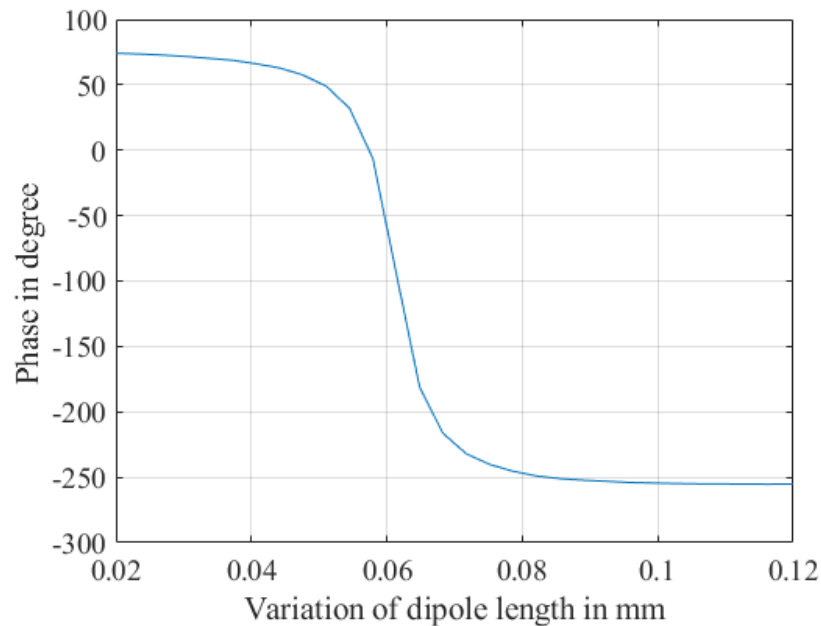


Figure 4.2: S-curve at 1.62 GHz

## 4.2 Design of the Cross Dipole Antenna Reflectarray

Given that the frequency of operation  $f = 1.62$  GHz, and the speed of light  $c = 3 \times 10^8$  m/s, the wavelength  $\lambda$  can be calculated as:

$$\lambda = \frac{c}{f} = \frac{3 \times 10^8}{1.62 \times 10^9} \approx 0.185 \text{ m} \approx 185.185 \text{ mm}$$

For a  $5\lambda \times 5\lambda$  reflectarray design at this frequency, there are approximately 7 unit cells in each direction. Therefore, the reflectarray is of dimension

$$\text{Desired dimension} = 7 \times 0.7 \times \lambda \approx 5 \times \lambda \text{ mm} \approx 908 \text{ mm}$$

Following the same approach detailed in section 3.2.1 and referring to the figure 3.7 , the vector  $\vec{r}_{mn}$  is formed as  $m\vec{a}_x + n\vec{a}_y$ , where  $\vec{a}_x$  and  $\vec{a}_y$  are the lattice vectors in the x and y directions, respectively. The maximum values of  $m$  and  $n$  are set to 7 each in this case. In this design,  $|F|$  is set to half the dimension of the reflect array antenna which equates to 454 mm.

The vector  $\vec{r}_i$  can be obtained by  $(\vec{r}_{mn} - \vec{F})$ . The phase  $\phi_{mn}$  at each cross dipole antenna is then a function of the vector  $\vec{r}_{mn}$ , given by the expression  $\phi_{mn} = k_0|\vec{r}_i|$ .

In the construction of the crossed dipole reflectarray antenna, the value of dipole length,  $L$  , for the design is determined from the S-curve shown in figure 4.2 and the conjugate of the phase  $\phi_{mn}$ . Note, the values of  $\phi_{mn}$  are also provided in Appendix A.2.

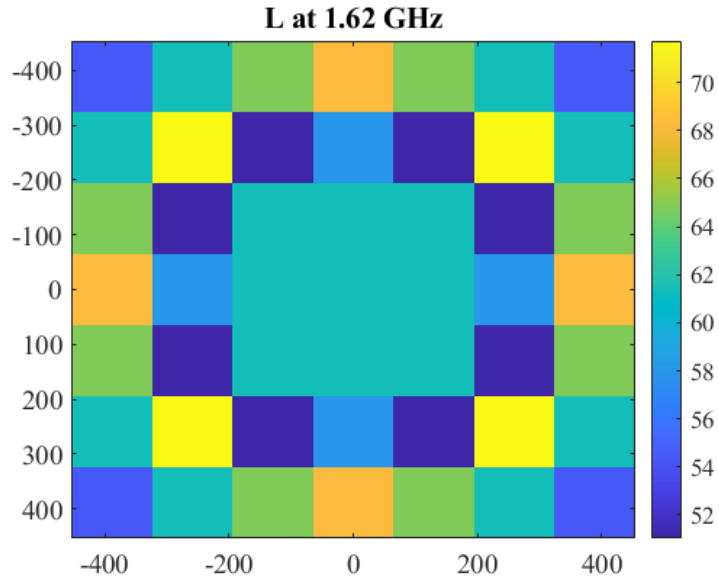


Figure 4.3: Analytical reflectarray model with the cross dipoles

The design of the crossed dipole reflectarray antenna is depicted in 4.3 with the dimension of  $L$  in the colorbar and the dimensions along the x and y directions in millimeters (mm).

### 4.2.1 Cross Dipole Reflectarray Working and Simulation

The analysis of the reflectarray is executed in CST MWS. Similar to the method in section 3.2.2, the macro facilities are utilised to draw the reflectarray and the raised cosine feed model is employed as the incident field for the reflectarray. The final CAD model is shown in figure 4.4.

After setting everything up, CST MWS was used to obtain the far fields.



Figure 4.4: Simulation of the cross dipole reflectarray model

Analysis of the far-field patterns reveal that the cross dipole reflectarray yields a colimated far field beam as shown in figure 4.5.

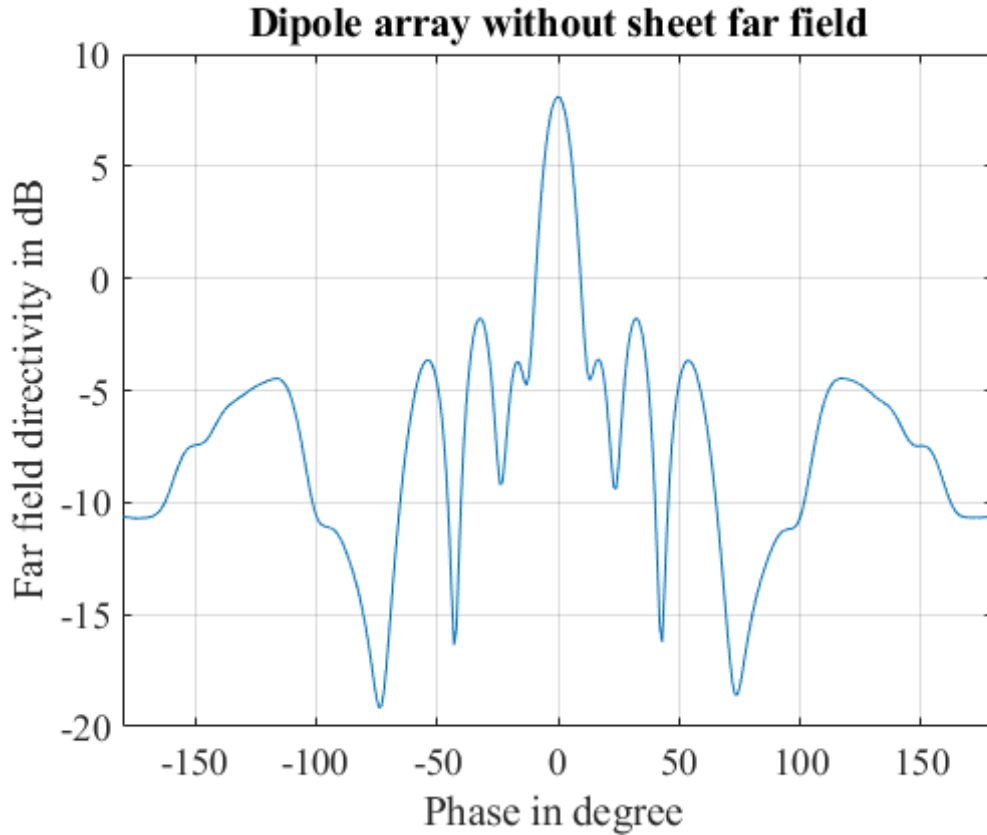


Figure 4.5: Co-polarized radiation pattern of cross dipole array model

This observation indicates that the unit cell structure has the capability to operate at a frequency of 1.62 GHz and the collimation of the field confirms the reflectarray's suitability for L-band applications.

Next, to achieve dual-band operation, it's necessary to integrate both the X and L-band layers together, with the X-band layer below the L-band layer and a PEC ground. The integration is discussed in the next chapter, chapter 5.

# Chapter 5

## Results and Discussions

### 5.1 Integration of the X-Band Layer to the L-Band Reflectarray at 1.62 GHz

This section explores the integration of the X-band layer and the L-band layer and shows the impact of integrating them into a single aperture when simulated at 1.62 GHz. *The metric for evaluating the effectiveness of this integration is the similarity in the pattern and directivity of the far-field radiation.*

Initially, the effect of slots on the L-band operation is examined. Subsequently, an equivalent homogenized sheet representing the slot layer is found. This equivalent model is necessary for computational efficiency. By developing the equivalent model, computational resources can be minimized while still retaining the accuracy necessary for the analysis.

#### 5.1.1 Simulation with the Slots without Homogenization

A cross dipole unit cell is placed on the X-band slot loaded reflectarray layer to evaluate its performance at 1.62 GHz shown in figure 5.1. For the analysis, the cross dipole antenna has been integrated onto a reflectarray composed of an array of  $14 \times 14$  unit cells of the X-band elements. As seen in 4.1.1, this number of cells gives a geometry which is closest to the dimension of the L band unit cell which is  $0.7\lambda$ . The simulation results provide S-curve within the L-band frequency with the slot loaded layer present.

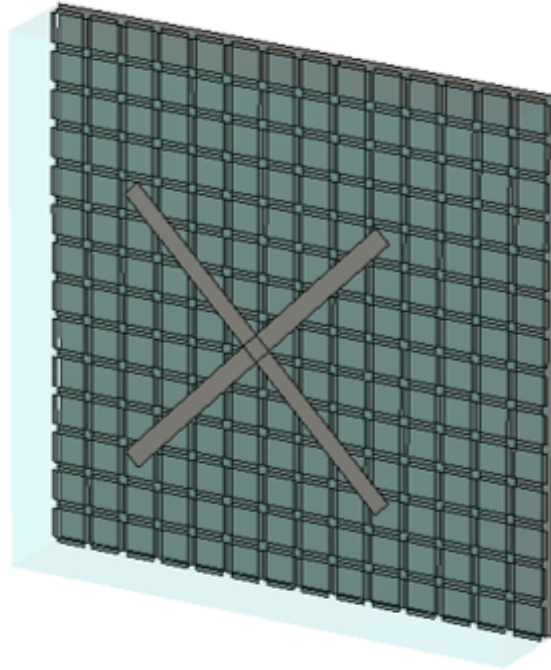


Figure 5.1: Dipole with slot-loaded unit cells at L band

### 5.1.2 Phase Analysis with Variable Slot Sizes

The variations in the phase of the reflection coefficient when the slot size of the X-band unit cells are changed is studied in this section. The plot, as shown in the figure 5.2, illustrates the phase response for different slot sizes of the unit cell, specifically for slots measuring 1.5 mm, 3 mm, and 6 mm.

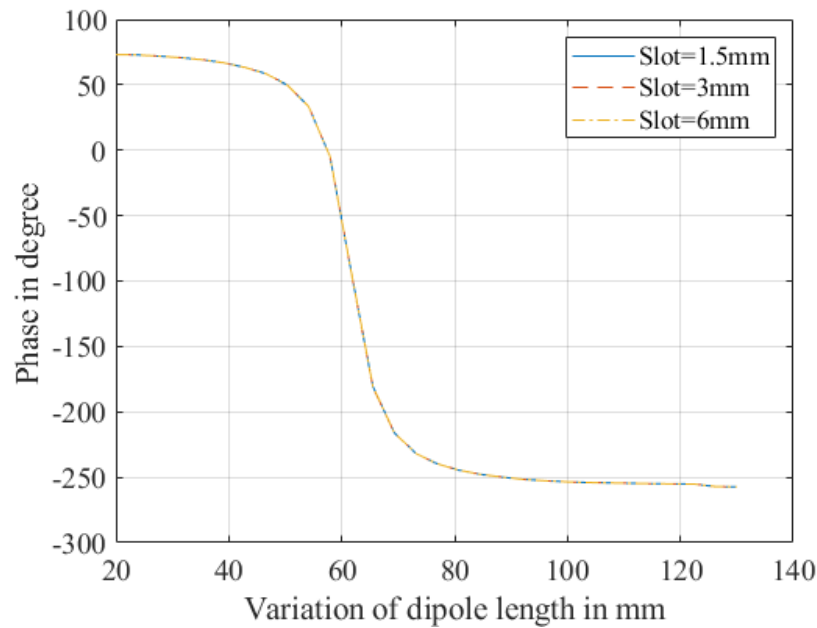


Figure 5.2: Phase response variation at 1.62 GHz with changes in the slot size of the X-band geometry.

The consistency in the S-curves is indicative of the fact that the L-band design will not be sensitive to changes in the slot dimensions of the X-band design. *Therefore, it can be concluded that the X-band slots do not affect the performance of the L-band reflectarray design consisting of cross dipole antennas.*

### 5.1.3 Homogenization of the Lower X-Band Layer as an Impedance Sheet

In this section, the slots within the X-band layer are homogenized at 1.62 GHz. This step permits the simulation of the reflectarray at L-band frequencies while mitigating the computational complexity introduced by the detailed slot geometry. *The goal for the homogenization of the slots therefore is to reduce computational burdens on the software.*

At L-band frequencies, the slot sizes do not have an effect on the L-band S-curve seen in figure 5.2 and hence can be effectively substituted by the equivalent impedance sheet.

This use of this model in simulation employs an impedance boundary condition where the impedance sheet is related to the ratio of the average electric field to the induced current density.

The model shown in figure 5.3 is analyzed using conventional transmission line theory.

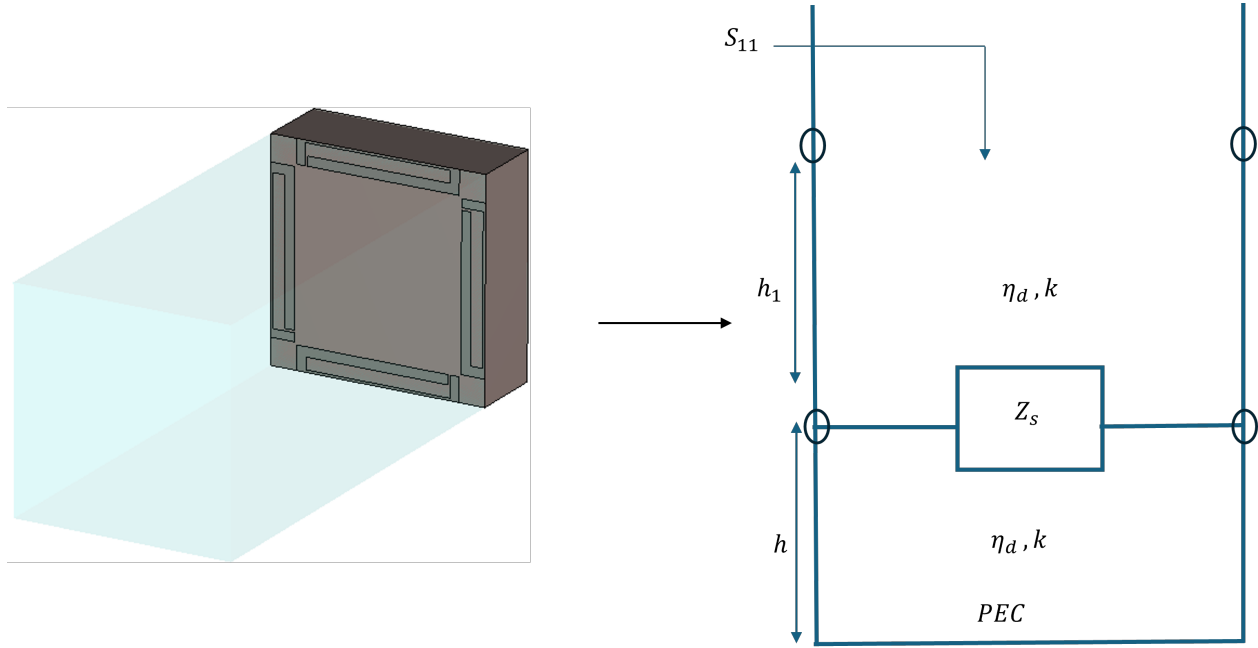


Figure 5.3: Slot-loaded unit cell conversion to Transmission line problem.

The calculation starts by considering the input impedance looking at the ground plane as shown in figure 5.3. Given the substrate width  $h = 3.175$  mm, the input impedance ( $Z_{in}$ ) is:

$$Z_{in} = jn \tan(kh)$$

Next, the sheet that is parallel to the input impedance is considered. The total load ( $Z_{load}$ ) is calculated using the following formula, which combines the sheet impedance ( $Z_s$ ) with the input impedance:

$$Z_{load} = \frac{Z_s \times Z_{in}}{Z_s + Z_{in}}$$

The superstrate width  $h_1$  is  $\frac{\lambda}{10}$  mm at the frequency 1.62 GHz.

The final input impedance ( $Z_{\text{in final}}$ ), as seen looking into the superstrate is given below:

$$Z_{\text{in final}} = \eta_d \left( \frac{Z_{\text{load}} + jn_d \tan(kh_1)}{\eta_d + jZ_{\text{load}} \tan(kh_1)} \right)$$

The reflection coefficient ( $S_{11}$ ) referred from [23] is calculated as:

$$S_{11} = \frac{Z_{\text{in final}} - \eta_0}{Z_{\text{in final}} + \eta_0}$$

Finally, to find the impedance value of the sheet ( $Z_s$ ), the above expressions are rearranged and solved for  $Z_s$ :

$$Z_s = \frac{\eta_d^2 \tan(kh) \tan(kh_1)(S_{11} - 1) - j\eta_0 \tan(kh)(S_{11} + 1)}{jn_d \tan(kh)(S_{11} - 1) + jn_d \tan(kh_1)(S_{11} - 1) + \eta_0(S_{11} + 1) - n_0 \tan(kh) \tan(kh_1)(S_{11} + 1)}$$

At a frequency of 1.62 GHz, the X-band unit cell with the superstrate shown in figure 3.3.1 is simulated in CST, and the  $S_{11}$  values are exported. Using the derived expressions mentioned above, the variations in impedance due to the varying slot lengths have been observed to be minor. Given this minimal fluctuation, it is considered appropriate to use the mean value for practical calculations.

Therefore, the impedance of the homogenized sheet has been determined to be approximately  $-544j$  ohms, as seen in figure 5.4.

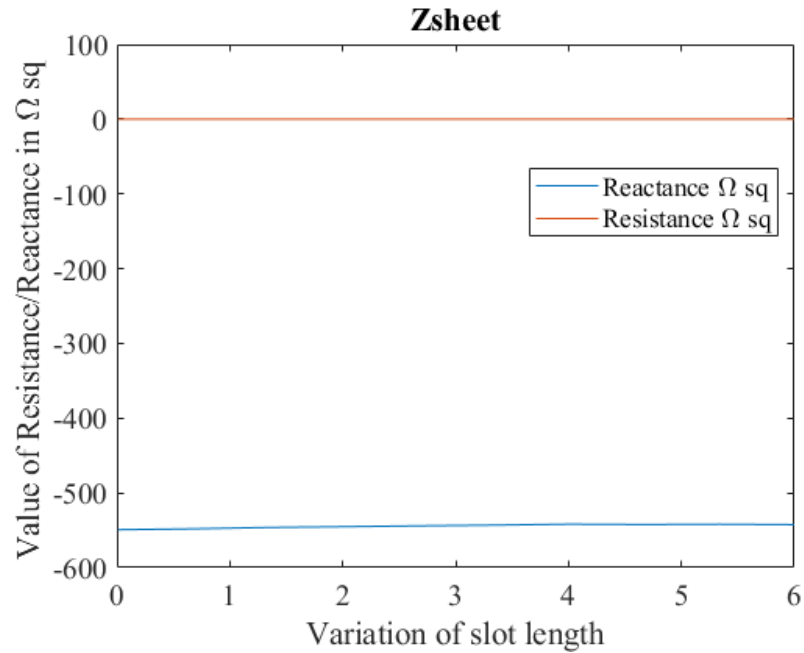
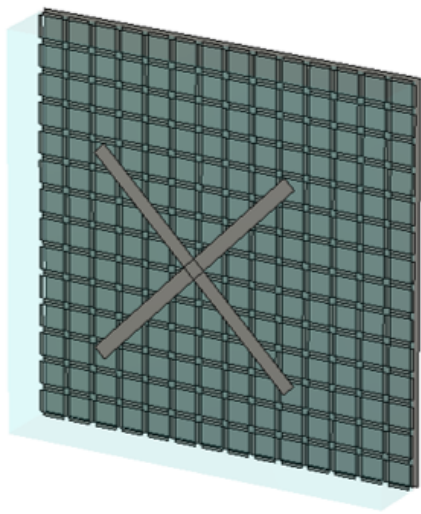
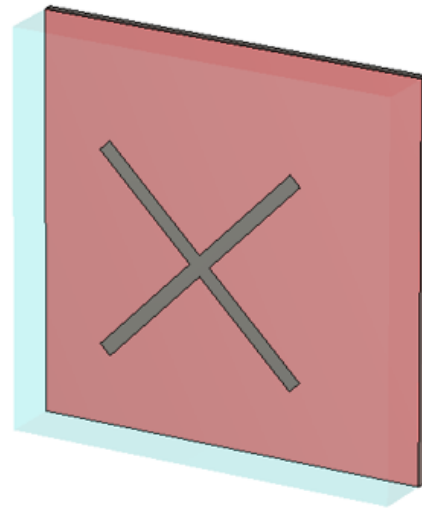


Figure 5.4: Impedance variation with the slot length

For further verification of the impedance sheet shown in the figure 5.4 , a cross dipole antenna is positioned above the X-band layer consisting of  $14 \times 14$  unit cell patches. This configuration is then compared with an analogous structure where the patches are substituted by an impedance sheet as shown in 5.5.



(a) Dipole with patches at L band



(b) Dipole with homogenized impedance at L band

Figure 5.5: Dipole antenna with X-band layer for one unit cell at L band

The S-curve results from the slots are compared with those from the homogenized sheet seen in figure 5.6.

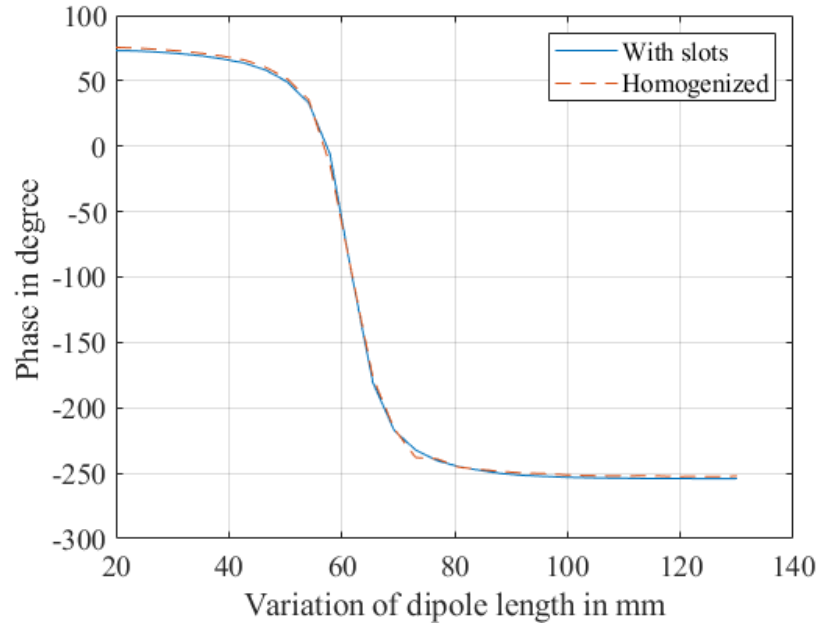


Figure 5.6: Comparison of the S-curves containing the slot-loaded unit cells and homogenized sheet.

The indistinguishable S-curves supports the design strategy at 1.62 GHz of replacing the slots by a homogenized sheet at this frequency .

*Summarizing, a homogenized sheet effectively replaces the slots thereby successfully reducing the computational burden of the CST microwave studio environment.*

#### 5.1.4 Design and Simulation of the Reflectarray with the Cross Dipoles and Homogenized Sheet

The design of the reflectarray follows the dimensions outlined in Section 4.2, which were chosen to be approximately  $5\lambda$  at 1.62 GHz.

The unit cell dimension at X band is 9 mm, and the total dimension of the reflect array

formed by 101 unit cells is shown below.

$$\text{Total dimension} = 101 \times 9 \text{ mm} = 909 \text{ mm}$$

*This closely matches the desired dimension of  $5\lambda$  at 1.62 GHz, making 908 mm a suitable size for the reflectarray.*

In this iteration of the design, the model incorporates a homogenized sheet to represent the X-band layer. As depicted in Figure 5.4, the value of the impedance sheet is  $-544j$  ohms. This sheet is positioned between the substrate and the superstrate, with the cross dipole array on top of the superstrate. This design is grounded using a Perfect Electric Conductor (PEC) as shown in figure 5.7.

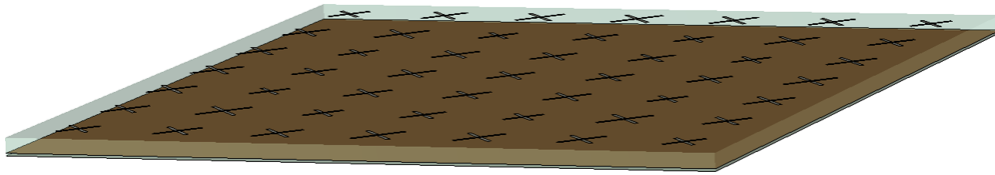


Figure 5.7: Reflectarray with cross dipole and homogenized sheet

Simulations to evaluate the far-field performance of the new model with a homogenized sheet representing the X-band layer, while comparing with the baseline model of the cross dipole antenna reflectarray (detailed in Section 4.2.1) is done. Notably, the presence of the homogenized sheet does not affect the far-field radiation patterns. Both configurations maintain a collimated beam.

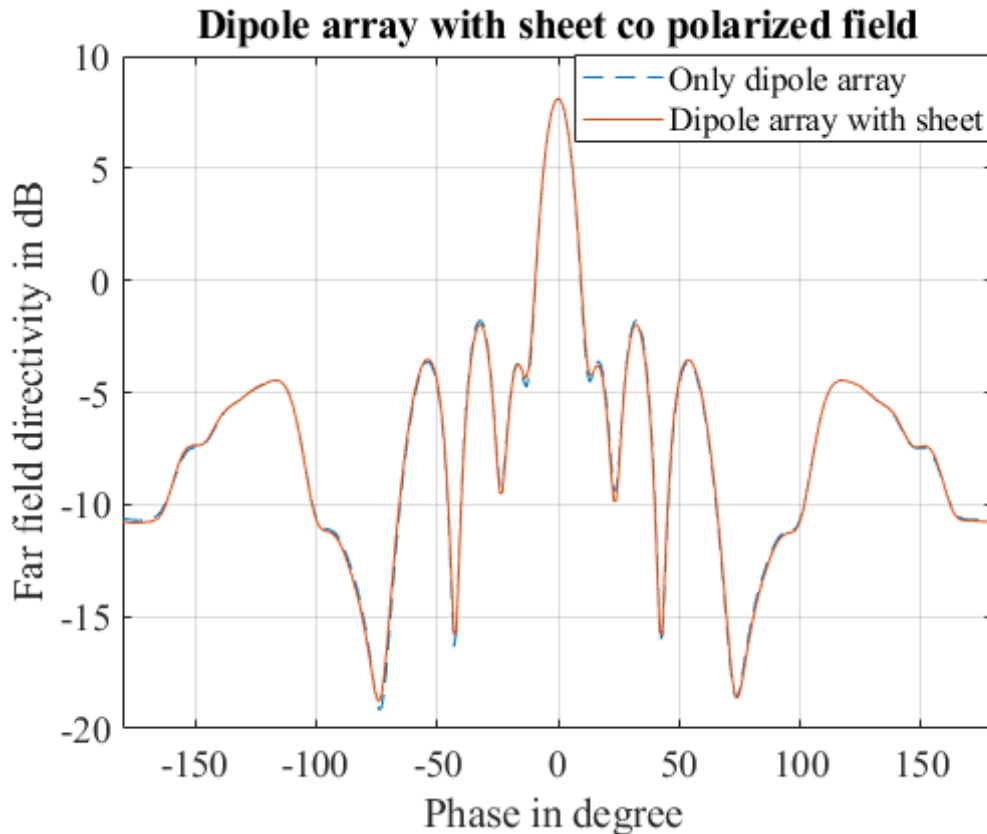


Figure 5.8: Comparison of the far-field patterns with and without the homogenized impedance sheet beneath the cross dipole reflectarray model.

*The results, as illustrated in figure 5.8, confirm that the introduction of the homogenized sheet into the cross dipole antenna reflectarray structure does not compromise the field's shape or directivity at the L-band.*

## 5.2 Integration of the L-Band Layer to the X-Band Reflectarray at 11 GHz

This section shows the effect of the integration of the L-band layer and X-band layers at X-band frequencies. The frequency considered is 11 GHz. The metric for evaluating the effectiveness of this integration is again the directivity and shape of the far-field radiation

pattern.

### 5.2.1 Design and Simulation of the Reflectarray with the Cross Dipole and Slot-Loaded Patches

The design and simulation focus on the frequency at X-band, 11 GHz, as outlined in Section 3.2. For this frequency, the effective dimension is identified as 135 mm, corresponding to  $5\lambda$ .

As detailed in Section 5.1.1, the simulation includes a cross dipole antenna placed above an array consisting of  $14 \times 14$  X-band unit cells. This aligns with the  $5\lambda$  dimension that consists of  $15 \times 15$  X-band unit cell patches. This supports the placement of one cross dipole antenna on the superstrate for the simulation as depicted in figure 5.9. This strategy is chosen based on its proportionality to the structure detailed in section 5.1.4.

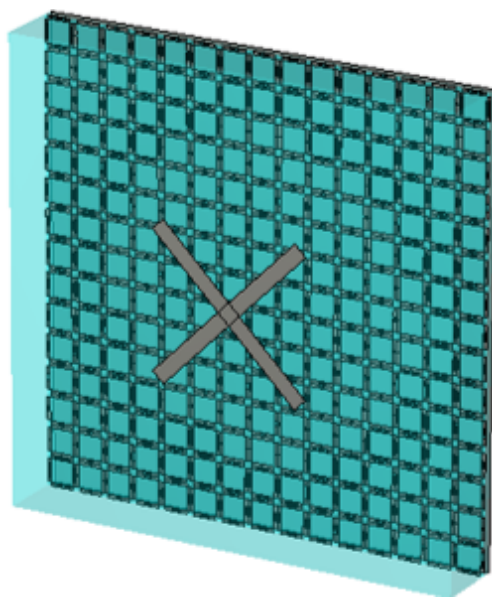


Figure 5.9: Simulation model illustrating the cross dipole antenna over the  $15 \times 15$  X-band unit cell patch array at 11 GHz.

### 5.2.2 Far-Field Performance

This section compares the far-field radiation patterns of the reflectarray under two conditions: with the array of patches and the superstrate from section 3.3.2, and subsequently, with the integration of a cross dipole antenna on the X-band patch antennas.

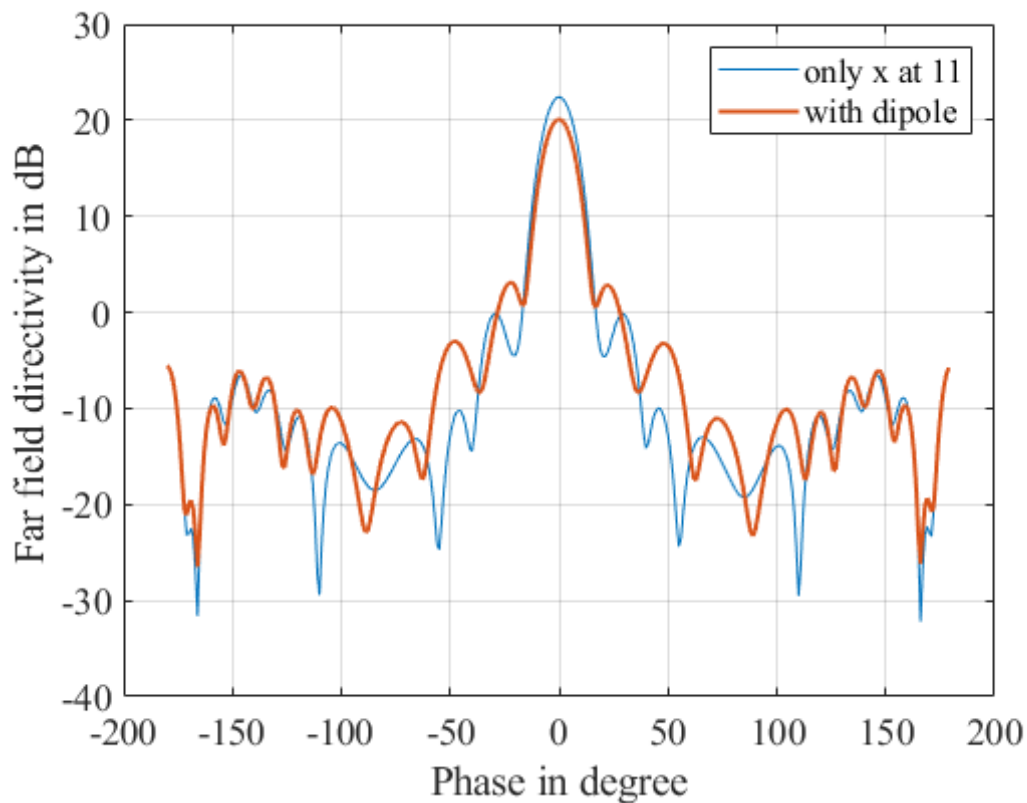


Figure 5.10: Comparison of the far-field patterns with and without the cross dipole antenna on the superstrate of the slot-loaded reflectarray

The integration of the cross dipole antenna introduces a blockage loss of approximately 2 dB in the far-field pattern as seen in figure 5.10. However, the directional properties of the radiation pattern, the main and side lobes, are preserved. This observation supports the conjecture that this reflectarray design could ultimately be used for interference mitigation applications in the future.

### 5.2.3 System Performance

According to the IEEE standards and definitions for antennas, aperture efficiency is defined as the ratio, usually expressed in percent, of the maximum directivity of an antenna [aperture] to its standard directivity.

Therefore, the aperture efficiency of an antenna can be calculated in terms of its maximum directivity using the formula:

$$\eta = \frac{D}{D_{\max}} \times 100$$

Where:

$\eta$  : Aperture efficiency

$D$  : Actual directivity of the antenna

$D_{\max}$  : Maximum possible directivity of the antenna

The formula of maximum directivity is,

$$D_{\max} = \frac{4\pi A_p}{\lambda^2}$$

where  $A_p$  represents the physical area of the antenna aperture and  $\lambda$  is the wavelength of operation.

The reflectarray antenna under investigation has the physical area ,  $A_p = 135 \times 135 \text{ mm}^2$  and  $\lambda = 0.0273 \text{ m}$  is the wavelength at 11 GHz. This thereby gives a maximum directivity of approximately 307 when evaluated in linear units.

Through the co-polarized far-fields obtained from CST Microwave Studio, it was ob-

served that the incorporation of the cross dipole onto the X-band layer yields a directivity of 20.1 dB, and when the cross dipole is not included has a directivity of 22.36 dB. Using these values, the aperture efficiency has been calculated using the above formulas. The results have been summarized in table 5.1.

Table 5.1: Reflectarray System Directivity and Efficiency

<b>Configuration</b>	<b>Directivity (dBi)</b>	<b>Efficiency (%)</b>
Without Cross Dipole	22.36	56
With Cross Dipole	20.1	35

However, it is important to emphasize that within the intended application of this thesis, the primary objective is not efficient beam collimation and rather is on destructive interference in the sidelobe region as part of null formation.

# Chapter 6

## Conclusion and Future Scope

The thesis is successful in the design and implementation of a reflectarray with dual-band and dual-polarization capabilities, specifically within the X(Starlink) and L(Iridium) bands.

### 6.1 Summary of this Thesis Contribution

The key findings are summarized as follows:

- Achievement of wideband performance at X-band frequencies (10.7 to 12.7 GHz), with a bandwidth of 17.1%, as detailed in Section 3.3.2, even after the addition of a superstrate as shown in figure 3.16.
- Demonstration in Section 4.2.1 that a cross dipole antenna array, when integrated with the model comprising of a superstrate, substrate, and grounded by a Perfect Electric Conductor (PEC), effectively produces controlled radiation at 1.62 GHz in the L-band as shown in figure 4.5.
- Integration and simulation of X-band slot loaded unit cells with L-band cross dipoles reflectarray design, as shown in Section 5.1.4 reveal that at the L-band, radiation patterns align well with and without the X-band layer. This is shown in the figure 5.8
- Integration and simulation of L-band cross dipole to X-band slot-loaded patches reflectarray design in 5.2.1, shows a slight reduction in efficiency seen in figure 5.10 and summarized in the table 5.1. However, the consistency in radiation patterns indicates

that the design remains effective.

- Finally note that the designs have symmetric geometry and thus respond equally to both linear-polarizations making them both dual-band and dual-linear polarized.

These imply the thesis's goals in attaining a dual-band dual-polarized reflectarray antenna with the required bandwidths is successful and can possibly be used in future applications for interference mitigation .

## 6.2 Future Scope

The findings from this thesis point to areas for further research. Here are some ideas for what could come next:

- **Make it Reconfigurable and Bigger:** The next step is work in attaining reconfiguration and figuring out how to design the antenna for reflector antenna interference mitigation scenarios.
- **Look at Dependence on Incident Angles:** It is important to see how the antenna does when signals imping upon it from wide angles. Future studies should check how changing the angle affects how well the antenna works, which could help make it better for real-life use.
- **Design for Both Bands Together:** Instead of making an antenna for one band and then adding the second band on top, designing it for both bands simultaneously could potentially enhance its efficiency.

# Appendices

# Appendix A

## Phases Requirements for the Reflectarray Designs

### A.1 Phase for the Reflectarray Design without Superstrate at X-Band

The phase information needed to build the reflectarray, outlined in section 3.2.1, is listed in table A.1. These values aid in the creation of the reflectarray structure showcased in figure 3.9. By incorporating this data into CST MWS to draw the reflectarray, we can simulate to obtain the co-polarized far-field.

In the table A.1, each row and column denotes the phase distribution across the unit cells at the X-band frequency range without the superstrate, arranged to form the reflectarray.

# Data Table of the Phase Desired ( $^{\circ}$ ) at X-Band without Superstrate:

Table A.1: Reflectarray Phase Distribution without the Superstrate at X-Band

Phase on Reflectarray Rows	Phase on Reflectarray Columns														
	1	2	3	4	5	6	7	8	9	10	11	12	13	14	15
1	-324.53	-28.08	-84.17	-131.85	-170.17	-198.27	-215.44	-221.21	-215.44	-198.27	-170.17	-131.85	-84.17	-28.08	-324.53
2	-28.08	-94.62	-153.61	-203.97	-244.60	-274.49	-292.80	-298.96	-292.80	-274.49	-244.60	-203.97	-153.61	-94.62	-28.08
3	-84.17	-153.61	-215.44	-268.45	-311.40	-343.11	-2.58	-9.15	-2.58	-343.11	-311.40	-268.45	-215.44	-153.61	-84.17
4	-131.85	-203.97	-268.45	-323.98	-9.15	-42.62	-63.24	-70.20	-63.24	-42.62	-9.15	-323.98	-268.45	-203.97	-131.85
5	-170.17	-244.60	-311.40	-9.15	-56.32	-91.39	-113.04	-120.36	-113.04	-91.39	-56.32	-9.15	-311.40	-244.60	-170.17
6	-198.27	-274.49	-343.11	-42.62	-91.39	-127.75	-150.24	-157.86	-150.24	-127.75	-91.39	-42.62	-343.11	-274.49	-198.27
7	-215.44	-292.80	-2.58	-63.24	-113.04	-150.24	-173.30	-181.11	-173.30	-150.24	-113.04	-63.24	-2.58	-292.80	-215.44
8	-221.21	-298.96	-9.15	-70.20	-120.36	-157.86	-181.11	-189.00	-181.11	-157.86	-120.36	-70.20	-9.15	-298.96	-221.21
9	-215.44	-292.80	-2.58	-63.24	-113.04	-150.24	-173.30	-181.11	-173.30	-150.24	-113.04	-63.24	-2.58	-292.80	-215.44
10	-198.27	-274.49	-343.11	-42.62	-91.39	-127.75	-150.24	-157.86	-150.24	-127.75	-91.39	-42.62	-343.11	-274.49	-198.27
11	-170.17	-244.60	-311.40	-9.15	-56.32	-91.39	-113.04	-120.36	-113.04	-91.39	-56.32	-9.15	-311.40	-244.60	-170.17
12	-131.85	-203.97	-268.45	-323.98	-9.15	-42.62	-63.24	-70.20	-63.24	-42.62	-9.15	-323.98	-268.45	-203.97	-131.85
13	-84.17	-153.61	-215.44	-268.45	-311.40	-343.11	-2.58	-9.15	-2.58	-343.11	-311.40	-268.45	-215.44	-153.61	-84.17
14	-28.08	-94.62	-153.61	-203.97	-244.60	-274.49	-292.80	-298.96	-292.80	-274.49	-244.60	-203.97	-153.61	-94.62	-28.08
15	-324.53	-28.08	-84.17	-131.85	-170.17	-198.27	-215.44	-221.21	-215.44	-198.27	-170.17	-131.85	-84.17	-28.08	-324.53

## A.2 Phase for the Reflectarray Design at L-Band

The phase information required for constructing the reflectarray, as detailed in section 4.2, is depicted in table A.2. These are values that help in the analytical construction of the reflectarray shown in figure 4.3 and is thereby used to finally draw it in CST MWS and obtain the co-polarized far-field pattern.

In the table shown in A.2, each row and column denotes the phase distribution across the unit cells at the L-band, which again forms the reflectarray containing the cross dipoles.

## Data Table of the Phase Desired ( $^{\circ}$ ) at L-Band with the Cross Dipoles

Table A.2: Reflectarray Phase Distribution at L-Band

Phase on Reflectarray Rows	Phase on Reflectarray Columns						
	1	2	3	4	5	6	7
<b>1</b>	20.14	-99.58	-177.18	-204.20	-177.18	-99.58	20.14
<b>2</b>	-99.58	-231.86	40.77	9.98	40.77	-231.86	-99.58
<b>3</b>	-177.18	40.77	-54.58	-88.57	-54.58	40.77	-177.18
<b>4</b>	-204.20	9.98	-88.57	-123.86	-88.57	9.98	-204.20
<b>5</b>	-177.18	40.77	-54.58	-88.57	-54.58	40.77	-177.18
<b>6</b>	-99.58	-231.86	40.77	9.98	40.77	-231.86	-99.58
<b>7</b>	20.14	-99.58	-177.18	-204.20	-177.18	-99.58	20.14

# Bibliography

- [1] HF AbuTarboush, HS Al-Raweshidy, and R Nilavalan. Bandwidth enhancement for microstrip patch antenna using stacked patch and slot. In *2009 IEEE international workshop on antenna technology*, pages 1–4. IEEE, 2009.
- [2] Constantine A Balanis. *Advanced engineering electromagnetics*. John Wiley & Sons, 2012.
- [3] Constantine A Balanis. *Antenna theory: analysis and design*. John wiley & sons, 2016.
- [4] Abdelheq Boukarkar and Rachdi Satouh. Bandwidth enhancement of compact patch antennas by loading inverted “l” and “t” strips. *International Journal of Microwave and Wireless Technologies*, 13(5):478–485, 2021.
- [5] Jordan Budhu, Sean V Hum, Steven Ellingson, and R Michael Buehrer. Design of rim-located reconfigurable reflectarrays for interference mitigation in reflector antennas. *IEEE Transactions on Antennas and Propagation*, 2024.
- [6] R Michael Buehrer and Steven W Ellingson. Weight selection for pattern control of paraboloidal reflector antennas with reconfigurable rim scattering. In *2023 IEEE Aerospace Conference*, pages 1–8. IEEE, 2023.
- [7] Steven Ellingson and Ramonika Sengupta. Sidelobe modification for reflector antennas by electronically reconfigurable rim scattering. *IEEE Antennas and Wireless Propagation Letters*, 20(6):1083–1087, 2021.
- [8] Mohammad-Hossein Golbon-Haghighi, Mirhamed Mirmozafari, Hadi Saeidi-Manesh, and Guifu Zhang. Design of a cylindrical crossed dipole phased array antenna for weather surveillance radars. *IEEE Open Journal of Antennas and Propagation*, 2:402–411, 2021.

- [9] Lu Guo, Peng-Khiang Tan, and Tan-Huat Chio. Bandwidth improvement of reflectarrays using single-layered double concentric circular ring elements on a subwavelength grid. *Microwave and Optical Technology Letters*, 56(2):418–421, 2014.
- [10] Lu Guo, Huiting Yu, Wenquan Che, and Wanchen Yang. A broadband reflectarray antenna using single-layer rectangular patches embedded with inverted l-shaped slots. *IEEE Transactions on Antennas and Propagation*, 67(5):3132–3139, 2019.
- [11] Chunhui Han, Yunhua Zhang, and Qingshan Yang. A novel single-layer unit structure for broadband reflectarray antenna. *IEEE Antennas and Wireless Propagation Letters*, 16:681–684, 2016.
- [12] Dale Hoffman. *Contemporary Calculus III*. Lulu. com, 2012.
- [13] John Huang and Jose Antonio Encinar. *Reflectarray antennas*. John Wiley & Sons, 2007.
- [14] Sean V Hum, Steven Ellingson, and R Michael Buehrer. Toward electronically reconfigurable rims for reflectors in radio astronomy. In *2023 XXXVth General Assembly and Scientific Symposium of the International Union of Radio Science (URSI GASS)*, pages 1–3. IEEE, 2023.
- [15] Sean Victor Hum and Julien Perruisseau-Carrier. Reconfigurable reflectarrays and array lenses for dynamic antenna beam control: A review. *IEEE transactions on antennas and propagation*, 62(1):183–198, 2013.
- [16] Steven L Johns and Aluizio Prata. An improved raised-cosine feed model for reflector antenna applications. In *Proceedings of IEEE Antennas and Propagation Society International Symposium and URSI National Radio Science Meeting*, volume 2, pages 970–973. IEEE, 1994.

- [17] David F Kelley and Warren L Stutzman. Array antenna pattern modeling methods that include mutual coupling effects. *IEEE Transactions on antennas and propagation*, 41(12):1625–1632, 1993.
- [18] Mohamed Latrach and Saiful Islam. Small broadband patch antenna design for l-band applications. In *2017 XXXIInd General Assembly and Scientific Symposium of the International Union of Radio Science (URSI GASS)*, pages 1–3. IEEE, 2017.
- [19] Shin-Rou Lee, Eng-Hock Lim, and Fook-Loong Lo. Broadband single-layer e-patch reflectarray. *Radioengineering*, 26(1):97–106, 2017.
- [20] Arthur Ludwig. The definition of cross polarization. *IEEE Transactions on Antennas and Propagation*, 21(1):116–119, 1973.
- [21] Derek H Maling. *Coordinate systems and map projections*. Elsevier, 2013.
- [22] Payam Nayeri, Fan Yang, and Atef Z Elsherbeni. Reflectarray antennas: theory, designs, and applications. 2018.
- [23] David M Pozar. *Microwave engineering*. John wiley & sons, 2011.
- [24] DM Pozar. Wideband reflectarrays using artificial impedance surfaces. *Electronics letters*, 43(3):1, 2007.
- [25] Yahya Rahmat-Samii and Joshua M Kovitz. Wideband e-shaped patch antennas for advanced wireless terminals. *Advanced Electromagnetics*, 12(2):1–19, 2023.
- [26] Warren L Stutzman and Gary A Thiele. *Antenna theory and design*. John Wiley & Sons, 2012.
- [27] A Vosoogh, K Keyghobad, A Khaleghi, and S Mansouri. A high-efficiency ku-band reflectarray antenna using single-layer multiresonance elements. *IEEE Antennas and Wireless Propagation Letters*, 13:891–894, 2014.

- [28] Ang Yu, Fan Yang, Atef Z Elsherbeni, John Huang, and Yahya Rahmat-Samii. Aperture efficiency analysis of reflectarray antennas. *Microwave and Optical Technology Letters*, 52(2):364–372, 2010.
- [29] Qiqi Zhou and Lu Guo. Design of a dual-polarized unit-cell for wideband reflectarrays. In *2021 IEEE International Workshop on Electromagnetics: Applications and Student Innovation Competition (iWEM)*, pages 1–3. IEEE, 2021.
- [30] Qiqi Zhou and Lu Guo. A multi-polarized metal-only reflectarray antenna. *IEEE Transactions on Antennas and Propagation*, 2023.
- [31] Qiqi Zhou, Lu Guo, and Wenjie Feng. A single-layered wideband circularly polarized reflectarray using a linearly polarized feed. *Microwave and Optical Technology Letters*, 65(4):955–960, 2023.
- [32] Zhibin Zou, Xue Wei, Dola Saha, Aveek Dutta, and Gregory Hellbourg. Scisrs: Signal cancellation using intelligent surfaces for radio astronomy services. In *GLOBECOM 2022-2022 IEEE Global Communications Conference*, pages 4238–4243. IEEE, 2022.